3-22-2019

Effects of Sinusoidal Phase Modulation on Signal-to-Noise Ratio in a Digital Holography System

Davin Mao

Effects of Sinusoidal Phase Modulation on Signal-to-Noise Ratio in a Digital Holography System

THESIS

Davin Mao, Capt, USAF

AFIT-ENP-MS-19-M-084

DEPARTMENT OF THE AIR FORCE
AIR UNIVERSITY

AIR FORCE INSTITUTE OF TECHNOLOGY

Wright-Patterson Air Force Base, Ohio

AFIT-ENP-MS-19-M-084

EFFECTS OF SINUSOIDAL PHASE MODULATION ON SIGNAL-TO-NOISE RATIO IN A DIGITAL HOLOGRAPHY SYSTEM

THESIS

Presented to the Faculty

Department of Engineering Physics

Graduate School of Engineering and Management

Air Force Institute of Technology

Air University

Air Education and Training Command

in Partial Fulfillment of the Requirements for the

Degree of Master of Science in Applied Physics

Davin Mao, B.S.Physics, M.S.E.E.

Capt, USAF

21 Mar 2019

AFIT-ENP-MS-19-M-084

EFFECTS OF SINUSOIDAL PHASE MODULATION ON SIGNAL-TO-NOISE RATIO IN A DIGITAL HOLOGRAPHY SYSTEM

THESIS

Davin Mao, B.S.Physics, M.S.E.E.
Capt, USAF

Committee Membership:

Dr. Glen P. Perram, Ph.D.
Chair

Dr. Christopher A. Rice, Ph.D.
Member

Dr. Mark F. Spencer, Ph.D.
Member

AFIT-ENP-MS-19-M-084

Abstract

Digital holography (DH) has been demonstrated to be an effective tool for tactical applications which involve in low signal-to-noise ratios (SNR). In practice, DH uses a strong reference beam from a local oscillator (LO) to scale SNR, however since DH relies on the interference of a signal beam with a mutually coherent LO, the coherence properties of the master oscillator (MO) can degrade system SNR for long range engagements. In this thesis, a digital holography system in the off-axis image plane recording geometry was assembled and used to measure the effects of the coherence properties of the MO on SNR. The coherence properties of the MO were degraded using sinusoidal phase modulation that imparted maximum phase shifts of $0.38\pi, 0.55\pi$, and 0.73π at modulation frequencies of 20 MHz to 100 MHz. A relative visibility-squared model was developed and used to predict the the measured efficiency losses. Predictions were computed both from the modulator specifications, and from measurements taken using a Fabry-Perot interferometer, and at best the measurements deviated from the predictions by root-mean-square errors of 0.0378, 0.0373, and 0.391 for depths of modulation $0.38\pi, 0.55\pi$, and 0.73π, respectively. Coherence efficiencies were measured at baseline SNRs of 75, 100, and 125 at the greatest depth of modulation, and it was found that the system's baseline SNR did not significantly impact the coherence efficiency in the high SNR regime. Overall, the empirical data and models presented in this work may be used to assess efficiency losses in a DH system due to coherence effects.

Acknowledgements

Friends. Family. Faculty.

Thank you,

Davin Mao

Table of Contents

List of Figures

List of Symbols

A_R	Reference amplitude
c	Speed of light
d	Fabry-Perot mirror displacement
$d_H^+(nx_p, my_p)$	Digitally recorded hologram
d_P	Pupil diameter
$\delta(x)$	Delta function
Δl	Optical path length difference
$\Delta\nu$	Full-width at half maximum
$\Delta\nu_{FSR}$	Free spectral range
$E(t)$, $E_1(t)$, $E_2(t)$	Arbitrary complex electric fields
E_0, E_1, E_2	Electric field amplitudes
$E_{mod}(t)$	Modulation signal
$\mathscr{E}\{\circ\}$	2-D Spatial expectation value operator
$\mathscr{F}$	Finesse
$\mathcal{F}\{\circ\}_{x,y}, \mathcal{F}^{-1}\{\circ\}_{\nu_x,\nu_y}$	2-D forward and inverse spatial Fourier transform operators
$\mathcal{F}\{\circ\}_{\tau}$	1-D temporal Fourier transform operator
$\gamma(\tau)$	Complex degree of coherence
$g_{A/D}$	Analog-to-digital converter gain coefficient
g_{amp}	Amplifier gain
g_{amp}^{dB}	Amplifier gain in dB
$\hat{\eta}_{coh}$	Relative Coherence Efficiency
η_{coh}	Coherence Efficiency
η_i	Efficiency of the ith loss factor
η_q	Quantum efficiency
η_{total}	Total efficiency

$i_H(x_2, y_2)$	Hologram irradiance
$\hat{i}_H(nx_p, my_p)$	Average hologram irradiance
I	Irradiance
$J_n(x)$	nth order Bessel function of the first kind
k	Angular wavenumber
$L(x)$	Lorentzian distribution function
λ	Wavelength
λ_π	Wavelength corresponding to half-wave voltage
$\overline{m}(nx_p, my_p)$	Mean hologram photoelectrons
$\overline{m}^+(nx_p, my_p)$	Hologram photoelectron distribution function
$\overline{m}_B(nx_p, my_p)$	Background mean photoelectrons
$\overline{m}_R(nx_p, my_p)$	Reference mean photoelectrons
$\overline{m}_S(nx_p, my_p)$	Signal mean photoelectrons
$n_k(nx_p, my_p)$	kth realization of unit-variance Gaussian random variable
(n, m)	Pixel index
N	Fourier plane noise energy
$N_1(x_1, y_1)$	Unit-variance complex-circular Gaussian random variable
p	Pixel width
$P(\omega)$	Power spectral density
$\mathcal{P}\{\circ\}$	Poisson-noise operator
$\phi(t)$	Time-variant phase
ϕ_0	Initial phase
q_I	Image plane sampling quotient
$\mathscr{R}$	Resolving power
S	Fourier plane signal energy
$S/N_{Fourier}$	Signal-to-noise ratio computed in Fourier domain

S/N_{IPRG}	Off-axis image plane recording geometry signal-to-noise ratio
S/N_{total}	Total signal-to-noise ratio
σ_I	Standard deviation of pupil estimate noise
σ_n	Standard deviation of Fourier plane pupil noise
σ_q	Standard deviation of quantization noise
σ_r	Standard deviation of read noise
σ_s	Standard deviation of shot noise
t	Time
τ	Propagation delay
τ_{int}	Integration time
$\theta(V_{in})$	Depth of phase modulation
$U_I(x_2, y_2)$	Image plane complex electric field
$U_P(x_1, y_1)$	Pupil complex electric field
$\hat{U}_P(x_1, y_1)$	Estimated pupil complex electric field
$U_P^+(x_1, y_1)$	Windowed pupil electric field estimate
$U_R(x_1, y_1)$	Reference complex electric field
$U_S(x_2, y_2)$	Signal complex electric field
V_{in}	Input voltage
V_{out}	Output voltage
V_π	Half-wave voltage
v	Visibility
$\hat{v}$	Relative Visibility
ν	Frequency
ν_0	Carrier Frequency
ν_m	Modulation Frequency
$\mathscr{V}\{\circ\}$	2-D spatial variance operator

$w(x_1, y_1)$	Window function
ω	Angular frequency
ω	Carrier angular frequency
(x_1, y_1)	Pupil plane coordinate system
(x_2, y_2)	Image plane coordinate system
(x_p, y_p)	Pixel pitch
x_R, y_R	Local oscillator x and y coordinates
z_I	Image distance
z_P	Object distance
$\circledast$	Convolution operator
$\otimes$	Cross-correlation operator
$\{\circ\}^*$	Complex conjugate operator
$\langle\circ\rangle$	1-D temporal expectation value operator

Introduction

Digital holography (DH) has a wide variety of applications including microscopy, imaging, and wave-front sensing due to its capability to encode and reconstruct the amplitude and phase of the complex electric field diffracted from a target object. In the remote sensing application, DH can be used to construct coherent (complex-valued) 2-dimensional (2-D) or 3-dimensional (3-D) images, and it can be used as a wave-front sensor for adaptive optics. Since DH relies on interfering a received signal with a mutually coherent reference to form an interferogram, the performance of the system at long range depends on the coherence length of the master oscillator (MO), from which both the reference and illuminator originate. In general, the round-trip distance to the target under interrogation should be less than the coherence length for DH using a continuous-wave (CW) source to be effective. Even if this requirement is satisfied, performance of the system degrades as distance to the target increases because the difference in optical path length between the signal and LO paths is increased. Degradation of system performance due to source coherence can be measured as a loss of signal-to-noise ratio (SNR) and quantified as a multiplicative system efficiency, namely the coherence efficiency. Thus, it is an important systems-engineering task to characterize the coherence efficiency of a DH system as the coherence efficiency dictates the operating range of the CW system. The primary goal of this effort is to isolate and quantify the effects of the temporal coherence properties of the source on the SNR of the DH system using experimental data.

When propagating light over 10s to 100s of kilometers, whether for imaging or directed energy applications, atmospheric effects become increasingly significant. Adaptive optics employs wave-front sensing techniques in order to correct phase aberrations due to atmospheric propagation. Digital holography has emerged as a viable alternative to the traditional Shack-Hartmann wave-front sensor, which performs

poorly in the presence strong scintillation [6, 7]. By estimating the phase function of the estimated complex wave-front, phase error correction techniques may be applied [18, 19, 27]. Extensive wave-optics simulations have been performed for DH implemented in various geometries to analyze their performance in the presence of strong turbulence. The performance of DH in the off-axis image plane recording geometry (IPRG) was simulated in [22, 23]. Similar simulations were performed for two other geometries, namely the off-axis pupil plane recording geometry (PPRG) [5] and the on-axis phase shift recording geometry (PSRG) [25]. While the simulations analyzed the performance of DH in the presence of deep atmospheric turbulence, the simulations assume a perfectly monochromatic, and therefore perfectly coherent source, which is unrealistic in practice. Long range DH experiments have been conducted at ranges of 100 m [16], however the authors state the "coherence length was significantly longer than the 200 m round trip path length and thus the return light and reference beam interfered coherently." Other 100 m range DH experiments were conducted with pulsed laser systems [15, 17], and in these experiments source coherence is not addressed.

Another advantage of DH is that its SNR can be scaled by increasing the power to the local oscillator (LO) that produces the reference field to remedy any efficiency losses. Interfering the signal with the LO couples the LO energy into the signal estimate, which is recovered using digital signal processing. A SNR model was developed in [10] for coherent detection. In general this model analyzed the effect of the spatial distributions of the reference and signal field over the detector surface. SNR models for each of the three DH geometries discussed above were derived in [21], and verified using wave-optics simulations [24]. A comprehensive survey of factors that cause efficiency losses in a DH system was conducted in [26] and validated experimentally, however efficiency losses due to coherence are not considered.

The effects of source coherence on DH have been examined in scenarios where the signal and reference path lengths are matched [8]. Here, the coherence requirement is defined by the size and depth of the target. The coherence efficiency was also considered in the context light detection and ranging (LIDAR [12]. The authors quantified the coherence efficiency with respect to the length of the integration window, which is different from the application discussed in this thesis. Regardless, the coherence theory applied will be similar to the ones discussed in [8] and [12].

There are applications in which degraded coherence of a source used for DH is desired. The effects of speckle, a consequence of coherent illumination, can be mitigated by decohering the light. In fiber laser applications, beam decoherence methods have been investigated as a solution to the problem of stimulated Brillouin scattering in [1, 2, 3]. The authors compared the effectiveness of phase modulating the source using pseudo-random, filtered pseudo-random, and white noise signals. The effects of using these phase-modulated beams for DH, however, is not discussed.

Although interferometry is at the heart of DH, the impacts of coherence on the SNR of a DH system have not been thoroughly investigated. Wave optics simulations assume a perfectly coherent source, and scaled-laboratory experiments are generally performed within the coherence length of the source, or use path length matching to overcome performance degradation due to coherence. This thesis presents data collected from a laboratory off-axis IPRG DH system which has the capability to degrade the source coherence in a controlled environment using an electro-optical phase modulator (EOPM) is used to sinusoidally modulate a 532nm CW laser source which is used as the MO for a digital holography system. The effects of the frequency of modulation and the amplitude of the applied phase shift on the SNR of the DH system are measured and analyzed within the framework of coherence theory.

The remainder of this thesis is structured as follows. Chapter II will present the

background information required to interpret the data collected for this thesis. Wavefront reconstruction using digital holography in the IPRG is presented in addition to a SNR model. Coherence theory is discussed and used to predict the coherence efficiencies that should result for a specific frequency and depth of modulation. In Chapter III, the DH system used to measure the data is introduced and data collection methods are discussed. Measured relative coherent efficiencies (RCE) are presented in Chapter IV, and conclusions are presented in Chapter V.

II. Background

Digital Holography

Holography is the two-step process of recording and reconstructing the electromagnetic field scattered from an object. Unlike photography, which records only the irradiance of the scattered field, holography recovers both amplitude and phase. Dennis Gabor, who developed the method in 1948 [11], originally called it "wavefront reconstruction." Many implementations of holography have been developed since its inception, each with different advantages and shortcomings. Common to all holographic techniques, however, are two fundamental steps: recording and reconstruction. In the recording step, coherent light scattered from an object is interfered with a mutually coherent reference on a transparent recording medium. Gabor called the recorded interference pattern a hologram, derived from the Greek "holos," meaning complete, and "gramme," meaning recording. In the reconstruction step, the hologram is illuminated with the same coherent reference used in the recording step. The original electromagnetic field scattered from the object can then be extracted from the field transmitted through the hologram.

Digital holography uses a focal plane array (FPA) instead of a transparent recording medium to digitally record the hologram [13]. In the reconstruction step, digital signal processing is used to recover the amplitude and phase of the field scattered from the object. Like holography, there are many implementations of DH. This thesis will focus specifically on the off-axis IPRG.

The following is a mathematical description of the recording and reconstruction steps used to implement DH in the off-axis IPRG. This description closely follows the more rigorous derivation given in [21].

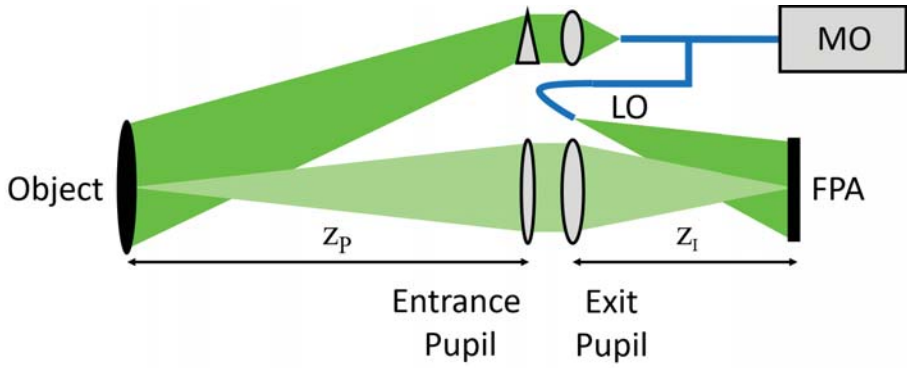

Figure 1. Digital holography in the off-axis image plane recording geometry. Coherent light from a master oscillator is split along two paths. The light on the signal path is collimated and used to illuminate a distant target. Light scattered from the target is imaged onto a focal plane array. The light diverted along the local oscillator path is redirected to the exit pupil plane and diverges from a position that is offset from the optic axis onto the FPA.

Figure 1 shows a diagram of the off-axis IPRG. In this application, a laser is used as the coherent source and is termed the MO. The beam from the MO is split into two paths that produce the illuminator and reference fields required for DH. Light along the illuminator beam path is collimated and optics are used to uniformly flood illuminate an object of interest. Light along the reference path is directed straight into the FPA and is termed the LO.

In Figure 1, digital holography is treated as a black box imaging system. Rays diverge from the plane of the object and propagate a distance z_P until they are intercepted by the entrance pupil where they are collimated. The collimated rays leave the imaging system from the plane of the exit pupil where they propagate a distance z_I before focusing to a point in the image plane where the FPA is positioned to record the hologram. It is important to note that the LO is located offset from the optical axis and positioned in the plane of the exit pupil. Physically offsetting the LO spatially offsets the complex pupil estimate from the other unwanted components in the Fourier plane, which enables wavefront reconstruction.

It can be shown that for such an imaging system the complex electric field in the

pupil plane, $U_p(x_1, y_1)$, and the complex electric field in the image plane, $U_I(x_2, y_2)$, form a Fourier-conjugate pair [21], and obey the relation

$$U_I(x_2, y_2) = \frac{e^{jkz_I}}{j\lambda_0 z_I} \exp\left(j\frac{k}{2z_I}(x_2^2 + y_2^2)\right)\mathcal{F}\{U_P(x_1, y_1)\}_{\nu_x=\frac{x_2}{\lambda z_I}, \nu_y=\frac{y_2}{\lambda z_I}}, \tag{1}$$

where $j = \sqrt{-1}$, λ_0 is the wavelength of the MO, $k = 2\pi/\lambda_0$ is the angular wavenumber, and z_P and z_I are the distances from the object to the entrance pupil and the exit pupil to the image plane, respectively. Here, coordinates (x_1, y_1) define a location in the pupil plane and coordinates (x_2, y_2) define the a location in the image plane. By convention, the z coordinate is coaligned with the optical axis. The coordinates (ν_x, ν_y) are Fourier plane spatial frequency coordinates. It is assumed that the spatial components of the electric fields are stationary over the timescale of interest so time dependences of the fields are omitted. This assumption is valid when the target is stationary or when the movement of the target is insignificant relative to the integration time of the FPA. The 2-D spatial Fourier transform operator $\mathcal{F}\{\circ\}$ is defined as

$$\mathcal{F}\{V(x, y)\}_{\nu_x,\nu_y} = \tilde{V}(\nu_x, \nu_y) = \int_{-\infty}^{\infty}\int_{-\infty}^{\infty} V(x, y)e^{-j2\pi(x\nu_x+y\nu_y)}dxdy, \tag{2}$$

and its inverse, $\mathcal{F}^{-1}\{\circ\}$, is defined as,

$$\mathcal{F}^{-1}\{\tilde{V}(\nu_x, \nu_y)\}_{x,y} = V(x, y) = \int_{-\infty}^{\infty}\int_{-\infty}^{\infty} \tilde{V}(\nu_x, \nu_y)e^{j2\pi(x\nu_x+y\nu_y)}d\nu_x d\nu_y. \tag{3}$$

The image of the object on the FPA is called the signal and its complex field,

$$U_S(x_2, y_2) = U_I(x_2, y_2), \tag{4}$$

can be used to obtain an estimate of the pupil plane complex field U_P, which is typically desired for wave-front sensing. Because $U_P(x_1, y_1)$ and $U_I(x_2, y_2)$ are Fourier

conjugate-pairs, if one field is obtained, the other can be computed using (2) or (3).

The reference field incident on the FPA due to the off-axis injected LO can be represented as the Fresnel approximation to a tilted spherical wave given by

$$U_R(x_2, y_2) = A_R e^{jkz_I} \exp\left[j\frac{k}{2z_i}(x_2^2 + y_2^2)\right] \exp\left[j\frac{k}{z_I}(x_R x_2 + y_R y_2)\right], \tag{5}$$

where A_R is a complex constant representing the LO electric field amplitude and (x_R, y_R) are the pupil plane coordinates of the off-axis LO.

The hologram irradiance incident on the FPA is the irradiance of the sum of the signal and reference fields expressed as

$$i_H = |U_S + U_R|^2 = |U_S|^2 + |U_R|^2 + U_S U_R^* + U_S^* U_R, \tag{6}$$

where the superscript * denotes the complex conjugate and the (x_2, y_2) dependences of the fields are omitted for compactness. The third and fourth term of (6) contain the desired U_S and its complex conjugate, U_S^*, but both terms are coupled to the reference field.

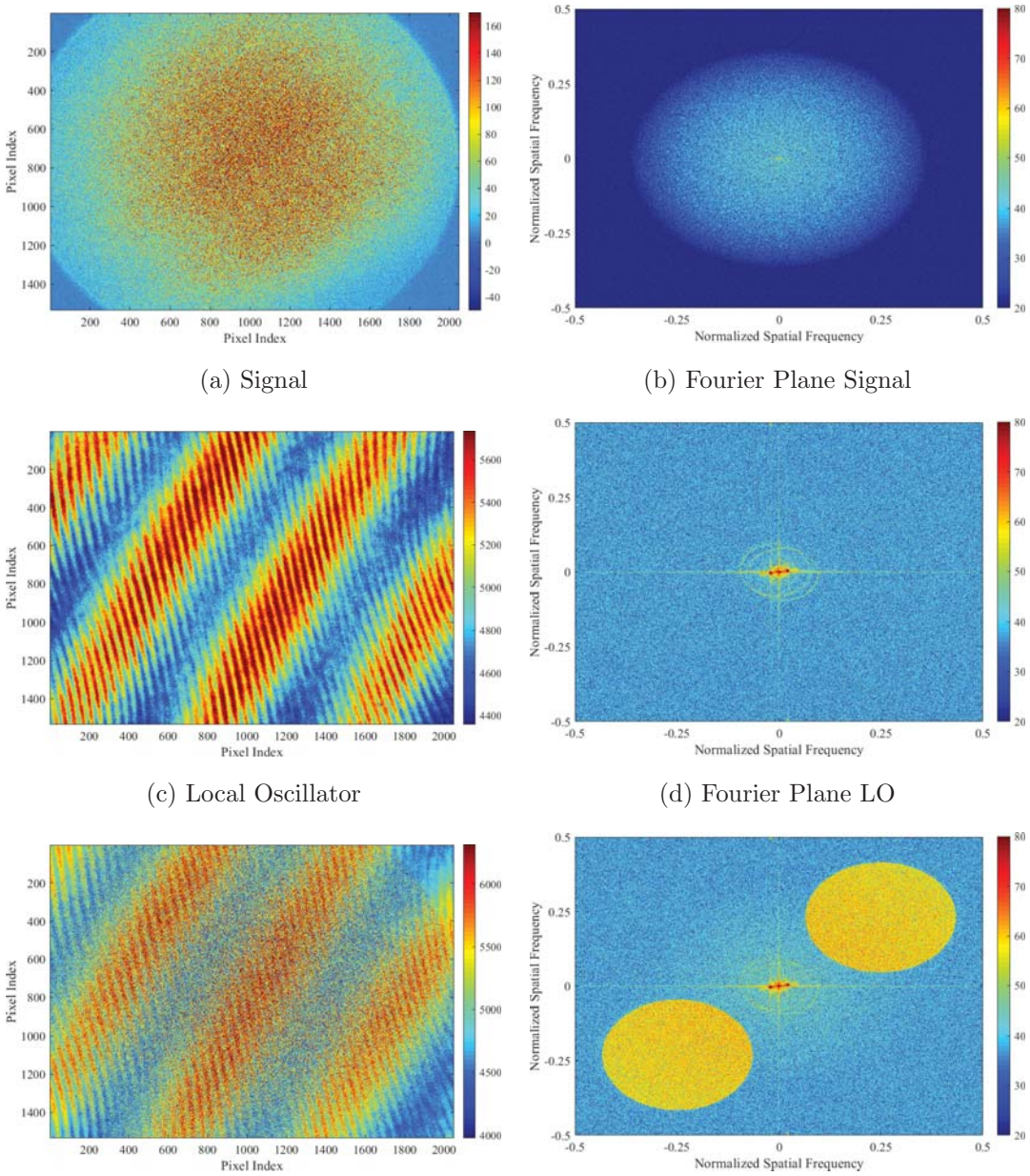

(a) Signal (b) Fourier Plane Signal

(c) Local Oscillator (d) Fourier Plane LO

(e) Hologram (f) Fourier Plane Hologram

Figure 2. (a) Signal Irradiance, (b) Signal Fourier Transform, (c) LO Irradiance, (d) LO Fourier Transform, (e) Hologram Irradiance, (f) Hologram Fourier Transform. Irradiance scale is in units of photoelectrons. Fourier plane scale is in dB. The signal is the image of a spectralon sample illuminated with a Gaussian beam. Speckle is observed. The local oscillator irradiance has displays fringes that are a consequence of the fiber stress rods and coherent imaging through the detector cover glass.

Figure 2 shows the recorded irradiances, (represented as photoelectron count (pe)) of the individual electric fields that compose the hologram (a,c), and the collected

hologram irradiance (e). Each image is an array of 1536x2048 pixels and is displayed in pe scale. The scale for each image spans 2 standard deviations above and below the mean pe count over all pixels in the image. The recorded signal irradiance (a) shows the image of a sample of spectralon that was flood illuminated with an expanded Gaussian beam. Speckle due to coherent imaging is present. The mean signal strength is 60±55 pe. The recorded LO irradiance (c) shows two sets of fringes that oscillate diagonally across the image. These fringes are not modelled by (21) and will be discussed in greater detail later. The mean LO irradiance is 5047±345 pe and is significantly stronger than the signal irradiance. Note, no pixels have value below 0 pe, despite the lower bound on the scale. Finally, the hologram irradiance in (e) is the sum of (a) and (c). Interference fringes are not easily visible due to strong speckle in the signal and the unwanted fringes in the LO. The hologram mean pe count is 5147±586 pe. The SNR of this hologram is 100.

Once the hologram is recorded by the FPA, U_S can be estimated using digital signal processing. To obtain U_S, the hologram irradiance is transformed into the Fourier domain. Substituting (4) and (5) into (6) and applying the inverse 2-D Fourier transformed defined in (3) using coordinate substitutions $x_2 = \lambda \mathrm{z}_I \nu_x$ and $y_2 = \lambda \mathrm{z}_I \nu_y$ gives

$$\begin{aligned}\mathcal{F}^{-1}\{i_H(\lambda_0 \mathrm{z}_I \nu_x, \lambda_0 \mathrm{z}_I \nu_y)\}_{x_1,y_1} &= \frac{1}{\lambda_0^2 \mathrm{z}_I^2} \tilde{i}_H\left(\frac{-x_1}{\lambda_0 \mathrm{z}_I}, \frac{-y_1}{\lambda_0 \mathrm{z}_I}\right) = \\ &\frac{1}{\lambda_0^2 \mathrm{z}_I^2} U_P(x_1, y_1) \circledast U_P(-x_1, -y_1) + |A_R|^2 \delta(x_1)\delta(y_1) \\ &+ \frac{A_R^*}{j\lambda_0 \mathrm{z}_I} U_P(x_1 - x_R, y_1 - y_R) - \frac{A_R}{j\lambda_0 \mathrm{z}_I} U_P^*(x_1 + x_R, y_1 + y_R),\end{aligned} \tag{7}$$

where $\delta(x)$ is the Dirac delta function. The symbol $\circledast$ denotes the 2-D convolution

operator defined such that

$$V(x,y) \circledast W(x,y) = \int_{-\infty}^{\infty}\int_{-\infty}^{\infty} V(x',y')W(x-x',y-y')dx'dy', \tag{8}$$

where x' and y' are dummy variables of integration.

To further the analysis, it is assumed that the pupil of the imaging system is a circular lens with diameter d_P so that the pupil plane complex electric field, U_P, has a finite region of support. The truncated pupil plane complex electric field is represented as

$$U_P(x_1,y_1) = w(x_1,y_1)P(x_1,y_1), \tag{9}$$

where $P(x_1,y_1)$ is a mathematical abstraction that represents the pupil plane complex electric field with infinite extent and $w(x_1,y_1)$ is the window function applied by the circular aperture. The window function is given by

$$w(x_1,y_1) = \mathrm{cyl}\left(\frac{\sqrt{x_1^2+y_1^2}}{d_P}\right), \tag{10}$$

where the cylinder function is defined as

$$\mathrm{cyl}(\rho) = \begin{cases} 1, & 0 \le \rho < 0.5 \\ 0.5, & \rho = 0.5 \\ 0, & \rho > 0.5. \end{cases} \tag{11}$$

By making the circular pupil assumption, the individual terms of (7) can be analyzed geometrically. The first term of (7) is a 2-D autocorrelation of the pupil plane electric field and is centered on-axis. Under the circular pupil assumption, the support of the autocorrelation term (where the term has non-zero values) is also a circular region with twice the diameter of the pupil. The second term contains separable on-axis

delta functions. The third and fourth terms contain off-axis amplitude-scaled copies of the desired complex pupil plane electric field, U_P, and its conjugate. The positions of the third and fourth terms depend on the physical location of the LO, (x_R, y_R), so it is possible for them to overlap with autocorrelation term in the Fourier domain. If overlap is undesired, the pupils can be shifted away from the autocorrelation term by physically displacing the injected LO farther from the optic axis, or it can be digitally subtracted [9].

Figure 3 shows the result of applying a 2-D spatial Fourier transform to the hologram irradiance. The twin conjugate pupil terms are located offset from the origin and centered at (x_R, y_R) and $(-x_R, -y_R)$. The separable on-axis delta functions are also present at the origin. Additional delta functions are due to LO fringes and are not included in (7), but will be discussed later. The autocorrelation term is also present but it is faint due to a weak signal relative to the LO. Figure 2 (b,d) shows the individual contributions to the Hologram Fourier domain from the signal and the LO. The autocorrelation term is easily visible in (b) when the strong reference is not present. It is clear that the autocorrelation has finite support in a circular region twice the size of the pupil. (d) shows that the on axis content in the Fourier domain is attributed to the LO only.

To extract the pupil plane electric field from (7), the desired pupil term is shifted and a window is applied to obtain

$$\begin{aligned} U_P^+ &= \tilde{i}_H\left(\frac{-x_1 - x_R}{\lambda_0 z_I}, \frac{-y_1 - y_R}{\lambda_0 z_I}\right) w(x_1, y_1) \\ &= \frac{A_R^*}{j\lambda_0 z_I} U_P(x_1, y_1), \end{aligned} \tag{12}$$

which can be inverted to obtain U_P.

It is important to note that the preceding treatment of the off-axis IPRG only

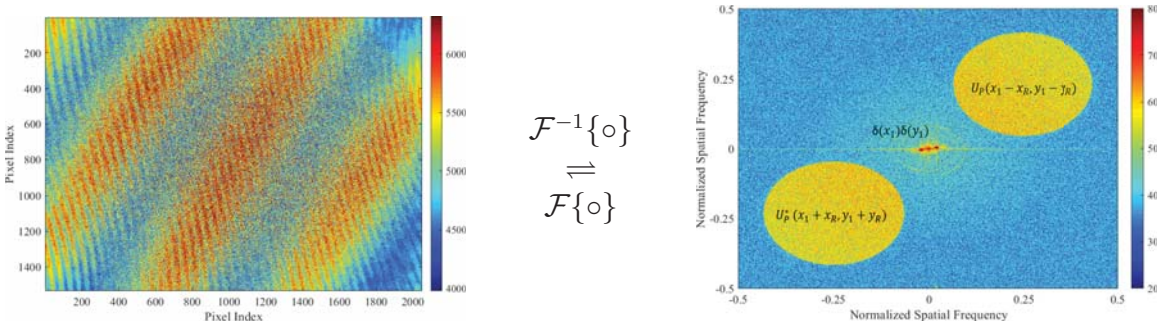

(a) Hologram Plane (b) Fourier Plane

Figure 3. Hologram and Fourier planes. (b) shows the twin pupil terms located off-axis from origin. Separable on-axis delta functions are visible. Additional delta functions are due to LO fringes. The on-axis pupil autocorrelation term is present but is faint due to weak signal.

addresses the qualitative steps required to estimate the pupil plane complex electric field from the hologram plane irradiance. In digital holography, the hologram plane irradiance is recorded by the FPA and converted into digital counts. The hologram irradiance must be properly sampled by the FPA to ensure unambiguous support in the Fourier plane when the recorded hologram is digitally transformed. An undersampled hologram may alias in the Fourier domain causing pupils in an adjacent Nyquist zone to spatially overlap with the desired estimate. A more rigorous treatment can be found in [21].

0.1 Fourier Analysis of Local Oscillator Fringes

Recall that LO irradiance in Figure 2 (c) displayed two sets of fringes, even though the LO is modelled as a flat field of uniform irradiance. There are two sets of fringes, 4 bright streaks that oscillate from the upper left corner to the bottom right corner of the image that shall be referred to the low spatial frequency fringes, and smaller oscillations that travel from the bottom left to the top right of the image, which shall be referred to as the high spatial frequency fringes. Figure 4 shows the magnified center of the LO Fourier plane shown in Figure 2 (d). The strong peak in the center

are the separable delta functions that are the expected result of flat field illumination. Immediately adjacent to the center delta are two very low spatial frequency deltas located at approximately (-0.001,0.0003) and (0.0017,-0.001). These deltas are oriented along the same axis as the low spatial frequency fringes.

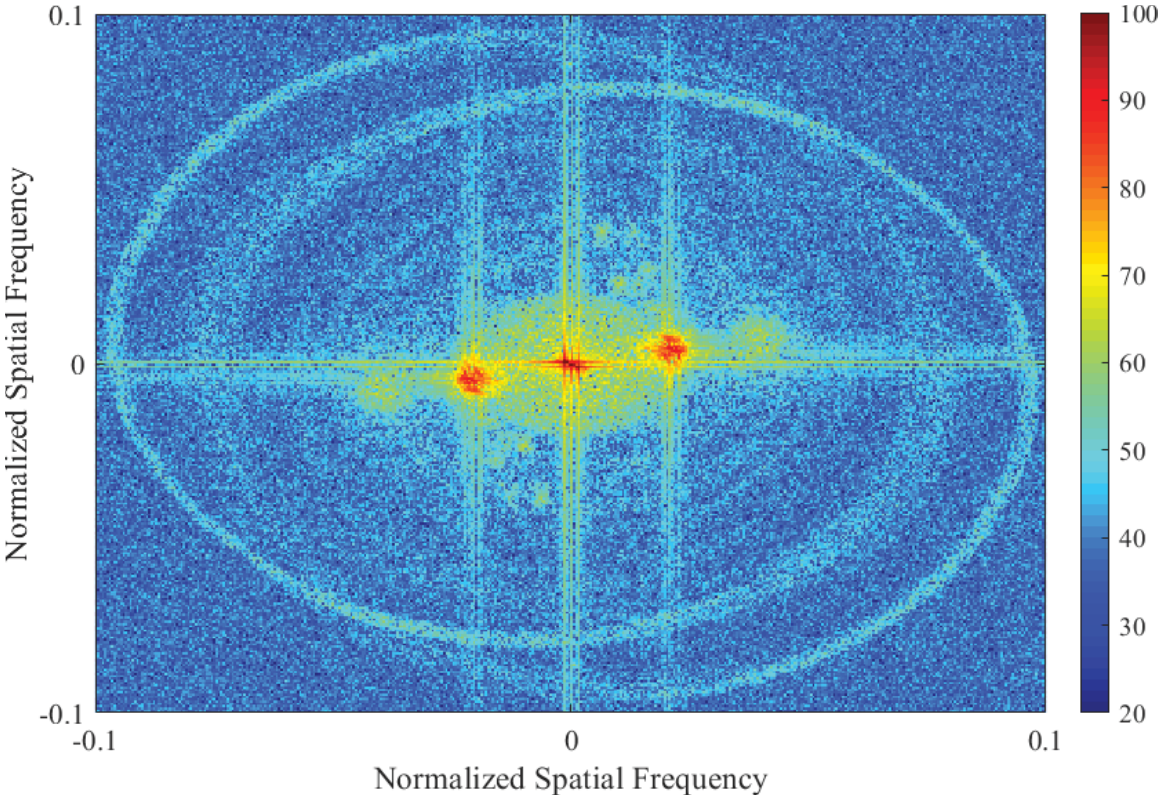

Figure 4. Magnified Fourier Domain Local Oscillator

Applying a circular notch filter over these two low frequency components as shown in Figure 5 (a) and taking the Fourier transform as shown in Figure 5 (b) completely removes the low spatial frequency fringes and leaves only the high spatial frequency fringes. Since the Fourier domain is the pupil plane of the imaging system, these spectral components must reside in the pupil plane. These low frequency components are likely due to "panda" configuration of the stress rods in the polarization-maintaining fiber. The separable on-axis deltas are the core of the fiber, the low spatial frequencies components are due to diffraction from the stress rods, and the remaining circular

region is the cladding of the fiber.

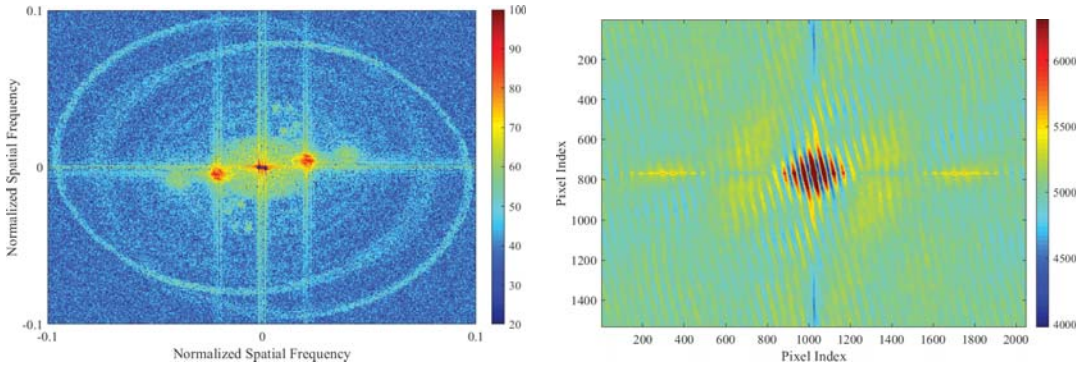

(a) Filtered LO Fourier Domain (b) Filtered LO Image Domain

Figure 5. (a) Fourier Domain Local Oscillator with Low Spatial Frequency Components Filtered Out, and (b) Image plane of filtered local oscillator.

The LO Fourier plane contains another set of strong high frequency components located at approximately (-0.02,-0.004) and (0.02,0.004). Applying a circular notch filter over these high spatial frequency components as shown in Figure 6 (a) and taking the Fourier transform as shown in Figure 6 (b) completely removes the high spatial frequency fringes and leaves only the low spatial frequency fringes. The high spatial frequency components are likely due to an "etalon" effect resulting from imaging through the camera coverglass. Evidence for this is in the fact that the spatial frequencies reside in the same quadrant as the pupil terms.

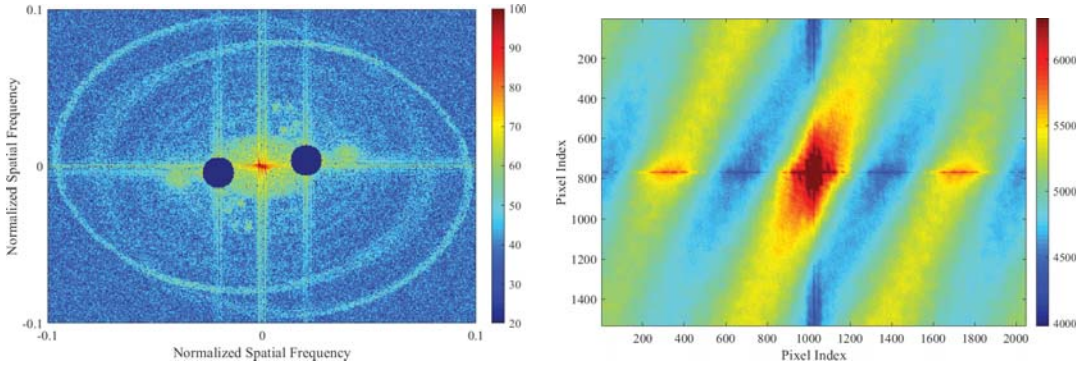

(a) Filtered LO Fourier Domain (b) Filtered LO Image Domain

Figure 6. (a) Fourier Domain Local Oscillator with High Spatial Frequency Components Filtered Out, and (b) Image plane of filtered local oscillator.

Finally, there are two off-center rings around the perimeter of Figure 4. It is suspected that these rings are a result of reflections off the retainer that holds the fiber tip in place. They are off center because the fiber is not situated in the center of the retainer, and there are two because the Fourier transform of a real valued quantity always has a conjugate.

Having characterized each source of the fringes in the LO Fourier domain, it is important to remember that during the wavefront reconstruction step, the pupil is windowed and the rest of the Fourier plane information is discarded. For the purposes of this thesis, the extraneous frequency components in the LO are inconsequential.

Signal-to-Noise Ratio

Analytic Model.

The SNR of the DH system in the off-axis IPRG is defined as

$$S/N_{IPRG} = \frac{\mathcal{E}\{|\hat{U}_P(x_1, y_1)|^2\}}{\mathcal{V}\{\hat{U}_P(x_1, y_1)\}}, \tag{13}$$

where $\hat{U}_P(x_1, y_1)$ is the pupil plane electric field estimated using DH. $\mathcal{E}\{\circ\}$ is the expectation value operator and $\mathcal{V}\{\circ\}$ is the variance operator, both computed spatially over two dimensions. To analyze SNR, this section departs from the deterministic model of the pupil plane electric field and treats the field as a stochastic system due to random arrival of photoelectrons on the FPA. If the field is oversampled by the FPA, the estimated pupil plane electric field can be approximated as

$$\hat{U}_P(x_1, y_1) \approx \frac{\eta \tau_{int}}{h\nu_0} p^2 A_R^* U_P(x_1, y_1) + \frac{\sigma_I}{\sqrt{2}} N_1(x_1, y_1), \tag{14}$$

where η is the detector quantum efficiency, τ_{int} is the detector integration time, h is Planck's constant, ν_0 is center frequency of the MO, p^2 is the area of an individual square pixel, σ_I is the estimate noise standard deviation, and $N_k(x_1, y_1)$ is the kth realization of a zero mean, unit variance complex-circular Gaussian random variable.

To further analyze the noise standard deviation, individual random processes that result in noise are identified. Again assuming square pixels with width p, the average irradiance at a pixel centered at $x = np$, $y = mp$ is

$$\hat{i}_H(nx_p, my_p) = \frac{1}{p^2}\int_{-\infty}^{\infty}\int_{-\infty}^{\infty} i_H(x', y')\text{rect}\left(\frac{x' - nx_p}{p}\right)\text{rect}\left(\frac{y' - my_p}{p}\right)dx'dy', \quad (15)$$

where x_p and y_p are the pixel pitches of the FPA and the rect function is defined as

$$\text{rect}(x) = \begin{cases} 1, & |x| < 0.5 \\ 0.5, & x = 0.5 \\ 0, & |x| > 0.5. \end{cases} \quad (16)$$

The mean number of photoelectrons incident on a pixel centered at $x = np$, $y = mp$ in the FPA then is

$$\overline{m}_H(nx_p, my_p) = \frac{\eta\tau_{int}}{h\nu_0}p^2\hat{i}_H(nx_p, my_p). \quad (17)$$

Assuming noise is additive [21], the random process can be characterized as

$$\overline{m}_H^+(nx_p, my_p) = \mathcal{P}\{\overline{m}_H(nx_p, my_p)\} = \sigma_r n_1(nx_p, my_p)\overline{m}_H(nx_p, my_p), \quad (18)$$

where $\mathcal{P}\{\circ\}$ is the Poisson-noise operator. The first term describes the random process associated with random arrival of photons on the FPA called shot-noise. The second term describes noise that is associated with the FPA circuitry called read-noise. In

the second term, σ_r is the read-noise standard deviation, and $n_k(x, y)$ is the kth realization of a real-valued, zero-mean, unit-variance Gaussian random variable.

Due to the presence of a strong LO, it is assumed that $\overline{m}_H(nx_p, my_p) \gg 1$, so that (18) may be approximated as

$$\overline{m}_H^+(nx_p, my_p) \approx \overline{m}_H(nx_p, my_p) + \sigma_s(nx_p, my_p)n_2(nx_p, my_p) + \sigma_r n_1(nx_p, my_p), \quad (19)$$

where σ_s is the shot-noise standard deviation. In this approximation, the Poisson random process is approxmiated as a Gaussian random process with variance equal to the mean, expressed as

$$\sigma_s^2(nx_p, my_p) = \overline{m}_S(nx_p, my_p) + \overline{m}_R(nx_p, my_p) + \overline{m}_B(nx_p, my_p), \quad (20)$$

where $\overline{m}_S(nx_p, my_p)$, $\overline{m}_R(nx_p, my_p)$, and $\overline{m}_B(nx_p, my_p)$ are the mean numbers of photoelectrons incident on the FPA due to the signal, reference, and background, respectively.

After the hologram irradiance is recorded by the FPA, the digital hologram can be expressed as

$$d_H^+(nx_p, my_p) = g_{A/D}\overline{m}_H^+(nx_p, my_p) + \sigma_q n_3(nx_p, my_p), \quad (21)$$

where $g_{A/D}$ is the gain factor that represents the number of counts recorded per detected photoelectron, and σ_q is the quantization-noise standard deviation associated with mapping of continuous energies to discrete counts. Assuming the analog signal can occur equally randomly anywhere between digital counts, the random process associated with quantization-noise can be characterized as a unit-width uniform dis-

tribution which has variance

$$\sigma_q^2 = \frac{1}{12}. \tag{22}$$

In the implementation of IPRG developed in the previous section, it was asserted that the reference field has uniform irradiance $|U_R(x,y)|^2 = A_R^2$ so $\overline{m}_R(nx_p, my_p) = \overline{m}_R$. Again invoking the strong reference beam assumption, it is further assumed that $\overline{m}_R \gg \overline{m}_S(nx_p, my_p)$, $\overline{m}_R \gg \overline{m}_B(nx_p, my_p)$, and $\overline{m}_R \gg \sigma_q/g_{A/D}$ so that the shot-noise variance in (20) reduces to $\sigma_S^2 \approx \overline{m}_R$. Further substitution of this approximation into (21) yields

$$d_H^+(nx_p, my_p) \approx g_{A/D}\big[\overline{m}_H(nx_p, my_p) + \sqrt{\overline{m}_R}n_2(nx_p, my_p) + \sigma_r n_1(nx_p, my_p)\big]. \tag{23}$$

Finally, (23) is divided by $g_{A/D}$ to obtain

$$\overline{m}_H^+(nx_p, my_p) \approx \overline{m}_H(nx_p, my_p) + \sigma_n n_4(nx_p, my_p) \tag{24}$$

which suggests that the arrival of photoelectrons on the FPA can be approximated as a Gaussian random process with a mean that depends on the strength of the reference and variance,

$$\sigma_n^2 \approx \overline{m}_R + \sigma_r^2, \tag{25}$$

that depends on the strength of the LO and detector read-noise variance.

Parseval's theorem suggests that the noise power in the hologram plane is conserved in the Fourier plane [21] so the noise standard deviation σ_n can be related to the variance of the pupil plane estimate, σ_I that appears in (13) by

$$\sigma_I^2 = \frac{\pi}{4q_I^2}\sigma_n, \tag{26}$$

where

$$q_I = \frac{\lambda z_I}{p d_P} \tag{27}$$

is called the image-plane sampling quotient and is the measure of the number of FPA pixels across the half-width of the point-spread function of the imaging system. The relationship described in (26) says that the variance of the electric field estimate is equal to σ_n times the ratio of the pupil area to the Fourier plane area.

Finally, having derived an expression for σ_I, the expression for SNR given in (13) can be expanded by acknowledging that the mean number of photoelectrons incident on the FPA due to the signal, $\overline{m}_S(nx_p, my_p) \approx \overline{m}_S$ is approximately constant and equal to

$$\overline{m}_S = \frac{\eta \tau_{int}}{h\nu_0} p^2 |A_S|^2, \tag{28}$$

where A_S is complex amplitude. Then

$$\mathcal{E}\{|\hat{U}_P(x_1, y_1)|^2\} \approx \overline{m}_R \overline{m}_S, \tag{29}$$

and

$$\mathcal{V}\{\hat{U}_P(x_1, y_1)\} \approx \sigma_I^2. \tag{30}$$

The expression for SNR can then be approximated as

$$S/N_{IPRG} \approx \frac{4q_I^2}{\pi} \frac{\overline{m}_R \overline{m}_S}{\overline{m}_R + \sigma_r^2}. \tag{31}$$

Lastly, in the limit where $\overline{m}_R \gg \sigma_r$, the SNR can be further reduced to

$$S/N_{IPRG} \approx \frac{4q_I^2}{\pi} \overline{m}_S. \tag{32}$$

This approximation is often called the shot-noise limit and is contingent on the as-

sumptions that $\sigma_r^2 << \overline{m}_r$ and that the FPA pixels are not saturated in the detection process.

Fourier Plane Signal-to-Noise Ratio Calculation.

The statistical models for SNR detailed above require knowledge of the deterministic complex electric field that is estimated, and a statistically sufficient number of realizations to characterize the noise data. An alternative method of computing SNR in the Fourier plane is presented that was used in [4].

Qualitatively, the technique takes advantage of the spatial separation of the of the twin pupil terms in the Fourier plane. The windowed pupil contains both the signal energy and the noise energy. The sum of the signal energy, S, and noise energy, N, is given by

$$\mathrm{S} + \mathrm{N} = |U_P^+|^2. \tag{33}$$

To isolate the signal energy, the window is reflected over one of the axes into an empty quadrant. The windowed empty quadrant is assumed to only contain noise. The isolated signal energy then is the expectation value of the windowed empty quadrant subtracted from the windowed pupil, given by

$$\mathrm{S} = \left\langle |U_P^+|^2 - |\tilde{i}_H\left(\frac{-x_1 - x_R}{\lambda_0 \mathrm{z}_I}, \frac{y_1 - y_R}{\lambda_0 \mathrm{z}_I}\right) w(x_1, y_1)|^2 \right\rangle. \tag{34}$$

Note the Fourier plane hologram is reflected before it is center-shifted because the Fourier transform of the real-valued hologram is symmetric in the spatial frequency domain.

The isolated noise energy is the expectation value of the windowed empty quadrant. The SNR, then is the ratio of the isolated signal energy to the isolated noise

energy, given by

$$\mathrm{N} = \left\langle \left| \tilde{i}_H \left(\frac{-x_1 - x_R}{\lambda_0 z_I}, \frac{y_1 - y_R}{\lambda_0 z_I} \right) w(x_1, y_1) \right|^2 \right\rangle. \tag{35}$$

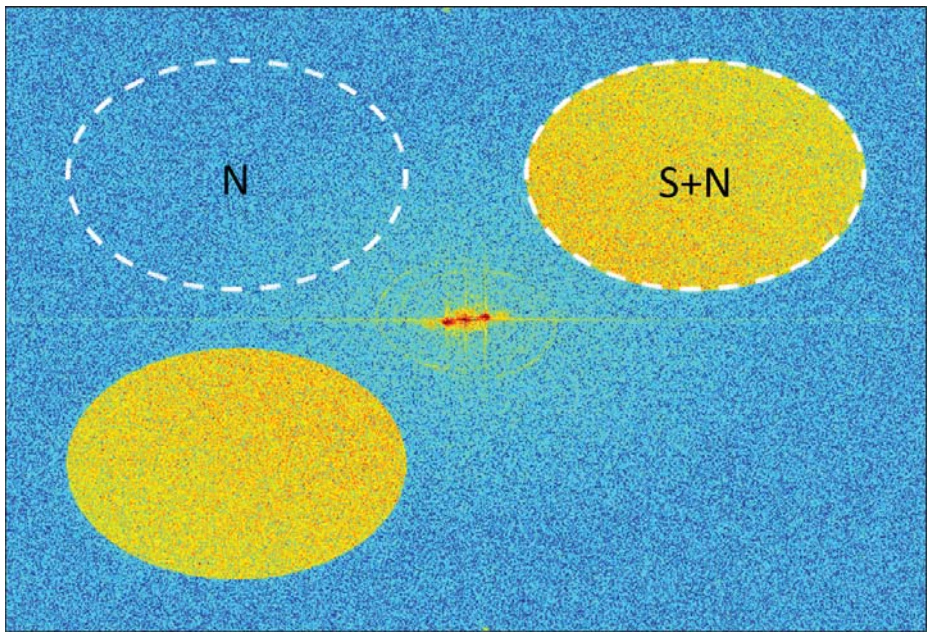

Figure 7. Fourier plane signal-to-noise ratio measurement. An empty noise quadrant is chosen and windowed to find a noise estimate.

Figure 7 shows the Fourier plane with white dashed lines illustrating the empty noise quadrant that is used to subtract noise from the pupil. Finally, the SNR is simply the ratio of the signal energy to the noise energy, expressed as

$$S/N_{Fourier} = \frac{\mathrm{S}}{\mathrm{N}}. \tag{36}$$

System Efficiency

There are several factors that can decrease the SNR of a DH system. Decreases in SNR due to the presence of these factors is called efficiency loss. While the mechanisms that cause these inefficiencies are generally complex, their impact on SNR can

typically be approximated as,

$$S/N_{total} = \eta_{total} S/N_{IPRG}, \tag{37}$$

where

$$\eta_{total} = \prod_i \eta_i \tag{38}$$

is the total system efficiency. Equation (38) suggests the total system efficiency is the product of all the individual sources of system inefficiency, η_i. As a convention $0 \leq \eta_i \leq 1$ where an efficiency of 1 is considered to be perfectly efficient and an efficiency of 0 is completely inefficient and completely degrades system SNR.

There are several sources of system inefficiences. A factor that has already been identified is the detector quantum efficiency, η_q, which accounts for the number of photons incident on the FPA that are converted into photoelectrons. Other efficiencies include, but are not limited to, the transmission efficiency, polarization efficiency, and coherence efficiency. Transmission efficiency is related to energy loss as light transmits through or is redirected by optics such as lenses, beam splitters, and mirrors. Polarization efficiency is due to the mismatching of the polarization states of the reference and signal paths of the DH system. In the case where a polarized MO is used and the signal beam is depolarized due to rough surface scatter, the polarization efficiency is 50%. A more complete list of sources of efficiency loss is compiled in [26].

Coherence efficiency is caused by the fact that a DH system relies on interference of the coherent reference beam with the mutually coherent signal beam. In the case where the MO is perfectly monochromatic and the reference and signal beam paths are exactly the same length, the coherence efficiency is 1. In practice, the spectral content of the MO has some width and the path length of the signal path, which must propagate to a distant target and back, is significantly longer than the path length

of the reference.

Coherence Theory

Coherence theory is discussed in this section. In particular, temporal coherence and its impacts on fringe visibility in an interferometer system is developed. Background on the Fabry-Perot interferometer is presented as a method to quantify the coherence of a signal. Finally, coherence will be tied back to the SNR of a DH system.

Temporal Coherence and Interference.

The following discussion of temporal coherence and interference is compiled from several foundational sources [14, 20, 28], however this discussion most closely follows the derivation done by [20].

For simplicity, the analysis begins with two arbitrary and purely monochromatic electric fields,

$$E_1(t) = E_1 \exp(j(\omega_0 t + \phi(t))) \tag{39}$$

and

$$E_2(t) = E_2 \exp(j(\omega_0(t+\tau) + \phi(t+\tau))), \tag{40}$$

that are made to superimpose at a single point. Here, E_1 and E_2 are the field amplitudes, $\omega_0 = 2\pi\nu_0$ is the field angular frequency, $\phi(t)$ is the time-variant phase of the fields, and τ is a time delay that is caused by a propagation optical path length difference (OPD) between the two fields.

The irradiance produced by the superposition of fields $E_1(t)$ and $E_2(t)$ is given

by,

$$\begin{aligned} I &= \langle |E_1(t) + E_2(t)|^2 \rangle \\ &= \langle |E_1(t)|^2 \rangle + \langle |E_2(t)|^2 \rangle + 2\mathrm{Re}\{\langle E_1(t)^* E_2(t) \rangle\} \\ &= E_1^2 + E_2^2 + 2E_1E_2\mathrm{Re}\{\langle e^{j[\phi(t+\tau)-\phi(t)+\omega_0 t]} \rangle\} \end{aligned} \tag{41}$$

where $\langle \circ \rangle$ is the temporal expectation value operator and $\mathrm{Re}\{\circ\}$ denotes the real part of a complex argument. While the first two terms are constant and depend on the field amplitudes, the third term depends on the propagation time difference, τ. The third term contains a quantity called the complex degree of coherence, which is expressed as

$$\gamma(\tau) = \langle e^{j[\phi(t+\tau)-\phi(t)+\omega_0 t]} \rangle. \tag{42}$$

The value of $\gamma(\tau)$ gives information about the coherence of the light source. For example $|\gamma(\tau)| = 1$ implies that the source is completely coherent whereas $|\gamma(\tau)| = 0$ implies that the source is completely incoherent. A value in between corresponds to a partially coherent source.

Using this new definition, the irradiance can be expressed as,

$$I(\tau) = E_1^2 + E_2^2 + 2E_1E_2|\gamma(\tau)|\cos(\arg\{\gamma(\tau)\}), \tag{43}$$

where $\arg\{\circ\}$ denotes the modulus of a complex argument. From (43), it can be seen that the irradiance takes on values between

$$I_{max} = E_1^2 + E_2^2 + 2E_1E_2|\gamma(\tau)| \tag{44}$$

and

$$I_{min} = E_1^2 + E_2^2 - 2E_1E_2|\gamma(\tau)|, \tag{45}$$

corresponding to path length differences that result in constructive and destructive interference. The measure of the fringe contrast of the interferogram is called the visibility and is expressed as,

$$v = \frac{I_{max} - I_{min}}{I_{max} + I_{min}} \tag{46}$$

$$= \frac{2E_1E_2}{E_1^2 + E_2^2}|\gamma(\tau)|, \tag{47}$$

which says that the fringe visibility is proportional to the complex degree of coherence.

Applying the above to DH, the arbitrary fields $E_1(t)$ and $E_2(t)$ are the signal beam and reference beam which both originate from the MO. Since light along the signal path must travel to a distant object and back, the reference path and signal path lengths will vary by some difference, Δl, which is related to the propagation time delay by $\Delta l = c\tau$, where c is the speed of light. Setting $E_1(t) = E(t)$ for the reference field and $E_2(t) = E(t+\tau)$ for the signal field and equating the second and third lines of (41), the complex degree of coherence for a DH system can be expressed as,

$$\gamma(\tau) = \frac{\langle E(t)^* E(t+\tau)\rangle}{\langle |E(t)^2|\rangle}. \tag{48}$$

The numerator of (48) is the time-domain autocorrelation of the electric field. Invoking the Wiener-Khinchin theorem, which states that the Fourier transform of the autocorrelation of the light field is proportional to the power spectrum of the source [20], yields the relationship

$$\mathcal{F}_\tau\{E(\tau) \otimes E(\tau)\} = \int_{-\infty}^{\infty} [E(\tau) \otimes E(\tau)] \exp(-j\omega\tau) d\omega = P(\omega), \tag{49}$$

where $\otimes$ denotes the 1D cross-correlation operator and $\mathcal{F}_\tau\{\circ\}$ denotes the 1-D tem-

poral Fourier transform operator, defined as

$$\mathcal{F}_\tau\{f(\tau)\} = F(\omega) = \int_{-\infty}^{\infty} f(\tau)\exp(-j\omega\tau)d\omega. \tag{50}$$

The quantity $P(\omega)$ is called the power spectral density (PSD) of the electric field and is a measure of the field's spectral content.

For a perfectly monochromatic source, the power spectral density of the electric field is a $P(\omega) = \delta(\omega - \omega_0)$. In practice, real sources have a finite bandwith. If a solid state laser is used as the MO, the power spectral density of the laser can typically be characterized by a Lorentzian distribution centered at the laser fundamental frequency ν_0. The Lorentzian distribution is given by

$$L(\nu) = \frac{\Delta\nu}{2\pi}\frac{1}{(\nu-\nu_0)^2 + (\Delta\nu/2)^2}, \tag{51}$$

where $\Delta\nu$ is the full-width at half maximum of the distribution.

Fabry-Perot Interferometer.

A Scanning Fabry-Perot Interferometer (SFPI) may be used as a spectrum analyzer to measure the power spectral density of a light source. The SFPI system used in this thesis consists of an etalon of two partially reflective mirrors separated by a distance d, a detector, a controller, and an oscilloscope to read the detector signal. Figure 8 shows a diagram of the system configuration.

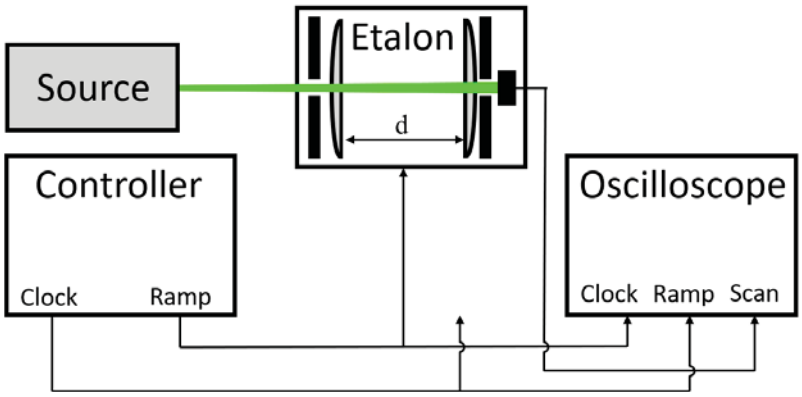

Figure 8. The scanning Fabry-Perot interferometer system consists of a Fabry-Perot etalon, controller, and oscilloscope. Light from a source enters the etalon of two partially reflective mirrors with curvature. The light self-interferes in the etalon cavity and the transmitted light is recieved by a detector on the back end and analyzed by an oscilloscope. One mirror is mounted on piezo-electric material that changes the cavity length, d, proportional to the applied voltage. The controller produces a saw-tooth ramp signal that is used to drive the piezo-electric material in the etalon, and a synchronized square wave that is used as a reference for the oscilloscope.

The source beam is directed into the etalon where the mirrors cause incident light to self-interfere. The irradiance resulting from the interference of the source is transmitted through the rear mirror and measured by a photodiode detector. The intensity of the measured interference fringe depends on the distance of separation of the mirrors and spectral content of the light source. A ramp voltage signal from the controller is used to drive a piezoelectric transducer on which one of the mirrors is mounted, which changes the separation distance of the mirrors in proportion to the applied voltage. As the mirrors scan to a separation distance of an integer multiple of half the wavelength, constructive interference occurs. Due to the periodic nature of the optical field, after the mirrors scan a certain distance, the pattern repeats. As such, a square-wave voltage signal is produced by the controller and used as a reference to synchronize the controller and the oscilloscope.

There are several important quantities that determine the performance of a SFPI.

For example, the coefficient of finesse [14],

$$F = \left(\frac{2r}{1-r^2}\right)^2, \tag{52}$$

depends on the reflectance of the mirrors, r. For highly reflective mirrors, F is typically very large, so it is more convenient to define the finesse of a SFPI as,

$$\mathscr{F} = \frac{\pi\sqrt{F}}{2}. \tag{53}$$

For a monochromatic source, the resulting interference pattern takes on the form of periodically repeating Gaussian distributions, and the finesse is the ratio of adjacent maxima to the half-width.

The finesse is related to the chromatic resolving power of the SFPI by

$$\mathscr{R} \approx \mathscr{F}\frac{2d}{\lambda_0}. \tag{54}$$

Finally, the free spectral range (FSR) is the distance between between two adjacent peaks in the scan and is given by

$$\text{FSR} = \frac{c}{4d} \tag{55}$$

for the Thorlabs SA 30-52 scanning Fabry Perot interferometer used in this thesis. The FSR is the unambiguous bandwidth measurable by the SFPI and a high FSR is required to measure sources with wide band spectral content.

Electro-Optical Phase Modulation.

An EOPM can be used to modulate the time-domain phase of an optical field. Figure 9 shows a diagram of the EOPM system used in this thesis.

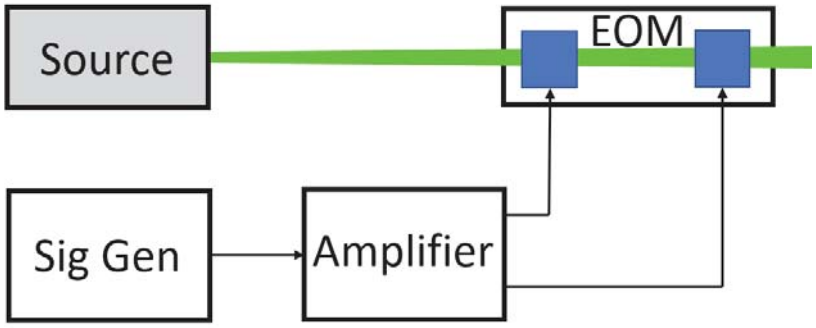

Figure 9. The electro-optical phase modulation system consists of an electro-optical phase modulator, signal generator, and analog amplifier. The signal generator produces the sinusoidal signal to be split and amplified by the amplifier. The amplified signal is used to drive crystals in the electro-optical phase modulator, which change index of refraction proportional to the applied voltage, modulating the phase of the incident beam.

The system consists of an electro-optical modulator, a signal generator, and an amplifier. The phase modulator contains two Lithium Tantalate (LTA) crystals that change index of refraction when a voltage is applied. The LTA crystals are suspended in index matching fluid to eliminate back reflections and are secured between electrodes and driven by a signal that originates at the signal generator. An amplifier is used to increase the voltage of the signal from the signal generator before it arrives at the EOPM.

The peak-to-peak voltage to the phase modulator that is required to induce a π phase shift is called the half-wave voltage, V_π, and is typically specified for some wavelength, λ_π. The half-wave voltage is approximately proportional to to wavelength, so the half-wave voltage at an arbitrary wavelength can be found using

$$V_\pi(\lambda) = V_\pi(\lambda_\pi)\frac{\lambda}{\lambda_\pi}. \tag{56}$$

An amplifier with gain G_{amp}^{dB} specified in dB, where

$$G_{amp}^{dB} = 20\log_{10}\left(\frac{V_{out}}{V_{in}}\right), \tag{57}$$

amplifies the signal input voltage according to

$$V_{out} = 10^{\frac{G_{amp}^{dB}}{20}} V_{in} = G_{amp}^{V} V_{in}. \tag{58}$$

Finally, the applied phase shift is proportional to the voltage applied to the EOPM, so the phase shift as a function of input voltage from the signal generated may be calculated using

$$\theta(V_{in}) = V_{in} G_{amp}^{V} \frac{\pi}{V_\pi} \frac{\lambda}{\lambda_\pi}. \tag{59}$$

The quantity, $\theta(V_{in})$, in addition to being the maximum phase shift that is imparted by the EOPM, is also referred to as the depth of modulation.

In this thesis, only sinusoidal phase modulation is investigated. In turn, consider the 1-D time-domain signal entering the phase modulator,

$$E(t) = E_0 \exp\{j[\omega_0 t + \phi_0]\}. \tag{60}$$

If the light is modulated using a sinusoidal signal with oscillation frequency ν_m defined by,

$$\phi(t) = \theta(V_{in}) \cos(2\pi\nu_m t), \tag{61}$$

then the resulting time-domain signal that emerges from the EOPM is given by

$$E_{mod}(t) = E_0 \exp\{j[\omega_0 t + \phi_0 + \phi(t)]\}. \tag{62}$$

The power spectral density of the resulting field can be calculated using the

Wiener-Khinchin theorem. For a perfectly monochromatic source, the power spectral density becomes a series of discrete lines located at $\nu = \nu_0 \pm n\nu_m$ (n = 0,1,2...) with amplitudes proportional to $J_n^2(\theta(V_{in}))$ where $J_n(x)$ is the nth order Bessel function of the first kind . If a source with spectral width, such as a Lorentzian distribution, is used in place of a monochromatic source, the lines are each replaced with an amplitude scaled Lorentzian distributions.

Visibility.

Assuming the source laser has a Lorentzian lineshape, if the MO linewidth and OPD between the signal and LO were known, a model of the PSD can be simulated for a specified frequency and depth of sinusoidal phase modulation. Taking the inverse Fourier transform of the simulated PSD yields the time-domain autocorrelation, which is proportional to the complex degree of coherence, and therefore to the visibility. Thus it is possible to compute a value for $v(\Delta\nu, \Delta l, \nu_m, \theta(V_{in}))$ that is accurate to a multiplicative constant. Further, if the computed value for the visibility was normalized to the visibility of an unmodulated signal, $v(\Delta\nu, \Delta l, \nu_m = 0, \theta(V_{in} = 0))$, the multiplicative factor is negated and the effect of the MO linewidth, which manifests as an exponential decay as a function of OPD, is also calibrated out. The relative visibility then is the normalized quantity,

$$\hat{v}(\Delta l, \nu_m, \theta(V_{in})) = \frac{v(\Delta\nu, \Delta l, \nu_m, \theta(V_{in}))}{v(\Delta\nu, \Delta l, \nu_m = 0, \theta(V_{in} = 0))}, \tag{63}$$

and is a function of the OPD, frequency of sinusoidal modulation, and depth of sinusoidal modulation only.

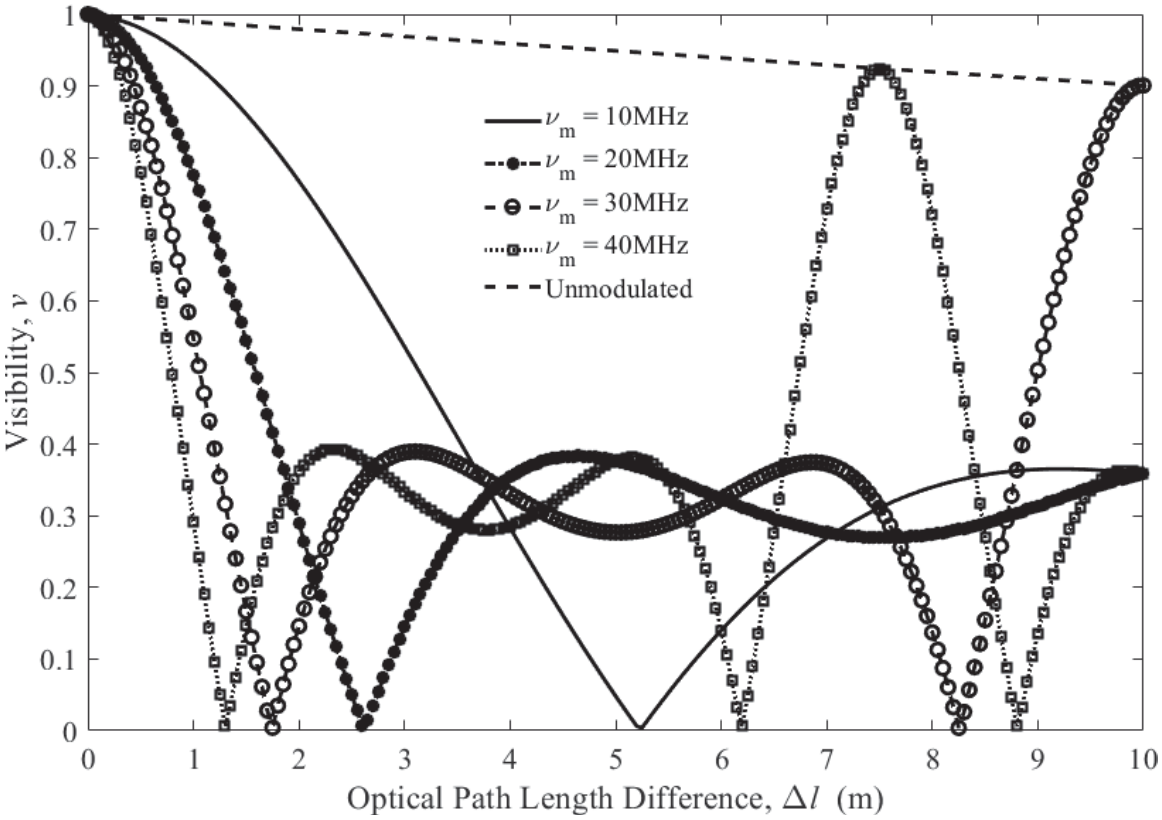

Figure 10. Simulated Visibility vs OPD at modulation frequencies ν_m = 0, 10, 20, 30, and 40 MHz. The modulation depth is $\theta(V_{in}$=1000 $mV_{pp})$=0.73π and the Lorentzian linewidth is $\Delta\nu$ =1 MHz.

Figure 10 shows the simulated visibility as a function of OPD and modulation frequency at a constant modulation depth of $\theta = 0.73\pi$ and an assumed linewidth of $\Delta\nu = 1$ MHz. The contribution of the linewidth is the exponential decay in the visibility of the unmodulated signal. The exponential decay curve is the Fourier transform of the Lorentzian distribution and is the upper bound on the visibility at a set path length difference for any given modulation frequency. To find the visibility as a function of modulation frequency from this plot, one need only draw a vertical line at the desired OPD, and find where it intersects each curve. This plot implies that for an OPD of less than 1 m, the visibility decreases monotonically as modulation frequency increases up to 40 MHz, however at longer OPDs the intersection of the curves become more chaotic. Interestingly, the first side lobe of the higher modulation

frequency curves appear at shorter OPDs. It is evident from this plot that it is difficult intuitively predict how modulation frequency will affect visibility for a an arbitrary OPD.

The fringe visibility in a digital hologram typically appears as a spatial sinusoidal amplitude modulation over the signal irradiance. However, in the presence of strong speckle, the fringes are difficult to see.

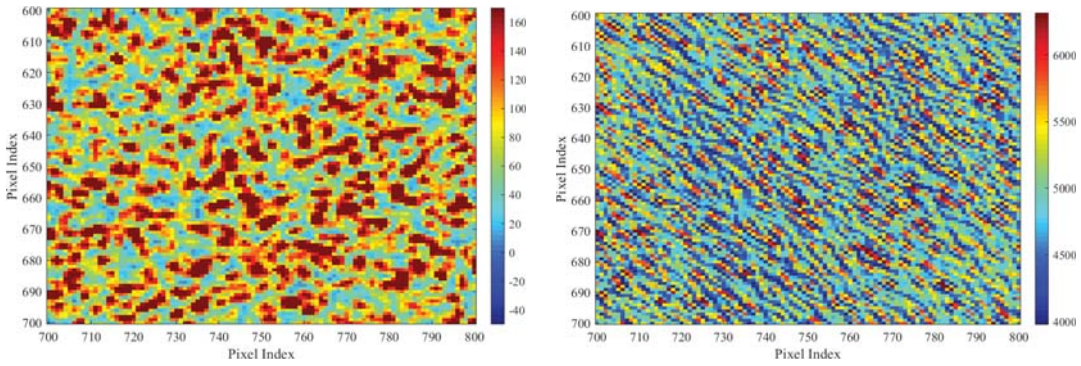

(a) Magnified Signal Irradiance (b) Magnified Hologram Irradiance

Figure 11. 100x100 pixel cropped region of the signal and hologram irradiances. Both scales are in units of photoelectrons.

Figure 11 (a) shows a 100x100 pixel region of the signal-only irradiance and Figure 11 (b) shows the same region of the hologram irradiance. Only speckle is observed in Figure 11 (a). In Figure 11 (b), the hologram fringes modulate the speckle. This figure is magnified enough that the fringes due to the LO are not observed, so the periodic amplitude modulation that runs from the bottom left corner of the image to the top right are the hologram fringes whose visibility are of interest. Figure 7 shows that the twin pupils are approximately centered on the first and third quadrant of the Fourier plane so their centers are located at $(\pm 0.25, \pm 0.25)$, suggesting that the normalized spatial frequency of the fringes is 0.25 per pixel. Inverting the frequency gives a spatial wavelength of 4 pixels. Close inspection of Figure 11 (b) reveals that the pixels are indeed spaced approximately 4 pixels apart (in fact, $4\sqrt{2}$ since the pupil

is on the diagonal).

III. Experimental Methods

This chapter describes the apparatus that was assembled to implement digital holography in the off-axis IPRG. In addition to digital holography, electro-optical modulators were installed in the optical path to manipulate the coherence properties of the MO and a SFPI was installed to analyze the extent to which the coherence properties of the MO were degraded. Finally, this chapter discusses the different modulation schemes under which data was collected using the DH system.

Digital Holography System.

Figure 12 shows a diagram of the DH system that was constructed to perform the efficiency measurements. A 532 nm Cobolt Samba 1000 laser was used as the MO. The Cobolt Samba is a diode-pumped solid state CW laser with a max power of 1 W with power stability that varies less than 2% over 8 hours. The Cobolt Samba produces a beam that is linear polarized vertically and has a polarization ratio of greater than 100:1. The beam waist is less than 300 μm and is located 20 cm in front of the aperture. The beam is in the TEM_{00} mode and has M^2 less than 1.1. The spectral linewidth is less than 1 MHz corresponding to a coherence length greater than 100 m.

A Thorlabs IO-5-532-HP visible free-space isolator was placed immediately after the MO to eliminate back reflections. The first half-wave plate (HWP), HWP1, and the first polarizing beam splitter (PBS), PBS1, were used to adjust the total power to the apparatus, and remove the unwanted energy into a beam dump.

An electro-optical amplitude modulator (EOAM) and EOPM were placed in the optical path to manipulate the coherence properties of the beam. The EOAM was a Conoptics Model 350-160 modulator and was operating as an EOPM with the output polarizer removed. The EOAM was not used in this thesis, but was installed

to support future DH coherence experiments. Its presence in the optical path did attenuate the transmitted beam due to a wavelength mismatch of the anti-reflective coating.

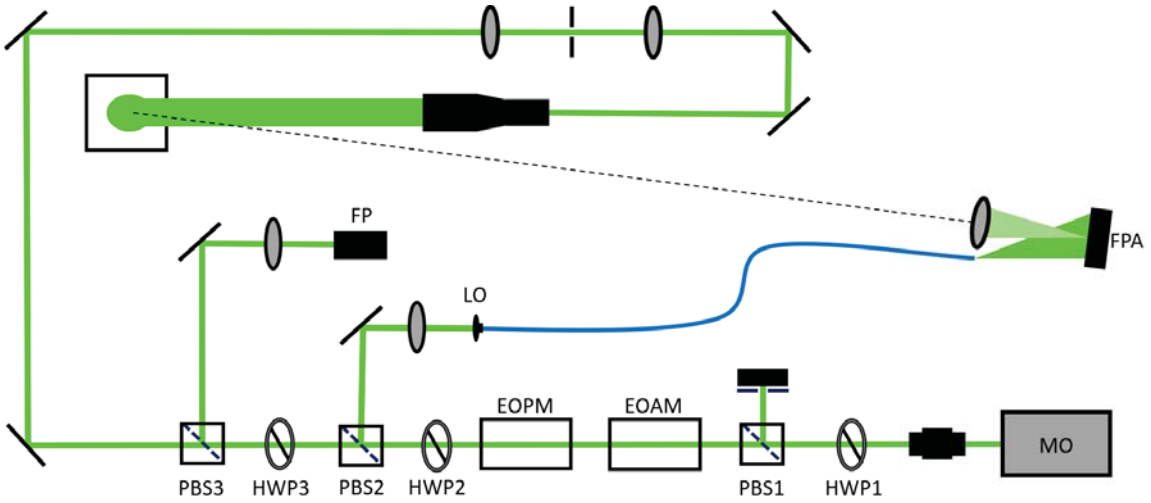

Figure 12. The digital holography system that was assembled to measure the effect of sinusoidal phase modulation on coherence. A 532 nm laser is used as the master oscillator and two phase modulators are placed in the optical path to degrade its coherence properties. Two subsequent beam splitters divert part of the phase-modulated beam to be used as the local oscillator and to be analyzed using a scanning Fabry-Perot interferometer. The transmitted signal is expanded and used to uniformly illuminate a sample of spectralon. The illuminated spot is imaged onto the focal plane array.

The entire EOPM system was composed of a Conoptics 360-40 modulator, a Conoptics Model 550 amplifier, and a Rohde and Schwarz RTO2044 oscilloscope signal generator module. The signal generator was used to drive the EOPM with a sine wave of various frequencies and phase shift amplitudes. Together the MO and EOPM simulate a MO with controllable coherence properties.

Following the EOPM, a second HWP and PBS combination (HWP2 and PBS2) was used to split off part of the source beam to use as the LO. A fiber coupler was used to inject the beam into a 2 m Thorlabs PC-155-PM-FC-2 polarization-maintaining FC/APC fiber optic cable that guided the beam to the pupil of the DH system. A retainer was used to install the output end of the fiber in the plane of the pupil of

the imaging system offset from the optical axis.

A third HWP and PBS combination (HWP3 and PBS3) was used to split off part of the source beam to analyze using a SFPI. A Thorlabs SA30-52 Fabry-Perot etalon with detector was used to measure the power spectral density of the beam. The SA30-52 has a FSR of 1.5 GHz and linewidth of less than 1 MHz. The SFPI was controlled using a Thorlabs SA201 spectrum analyzer controller and analyzed using the same Rohde and Schwarz RTO2044 oscilloscope used to drive the EOPM. The FPI was only used to verify the effectiveness of the EOPM and was never used during hologram collection. A beam block was placed between PBS3 and the SFPI during data collection to prevent back reflections from propagating into the LO fiber coupler.

The remaining source beam that propagated through PBS3 was used to flood illuminate a sample of spectralon with 99% Lambertian reflectivity. Because of beam expansion due to the longer optical path, a two lens and pinhole system was used to refocus the beam. A Thorlabs GBE20-A 20X beam expander was used to expand the beam before illuminating the spectralon. The expanded beam formed a 6$\pm$0.5 cm spot on the spectralon which was the target of the DH system.

A lens was used to image the target onto the a FLIR Grasshopper3 CMOS camera. The camera has a 2048x1536 pixel array with 3.45 μm square pixels. The camera was operated in mode 7. In mode 7, the integration time was 1 msec, the read noise variance was 5.5 pe^2, and the quantization noise variance was less than 1 pe^2. No digital non-uniformity was applied to the data collected using this camera. While the camera originally had two protective coverglasses in front of the FPA, the front coverglass was removed to mitigating an etalon effect caused by imaging a coherent source. The FPA was controlled by a laptop using Matlab-based software.

The OPD between the LO and signal paths, measured from PBS2 to the imaging

lens in front of the FPA, was 3.14±0.20 m. The combination of measuring the multiple legs that made up the signal path and computing the optical path length of the 2 m fiber resulted in a relatively large uncertainty in the estimated .

Data Collection and Processing.

This section describes the data collection procedure used in this experiment. Three independent variables were investigated for their impact on coherence efficiency: 1) the depth of the sinusoidal modulation, $\theta(V_{in})$, 2) the frequency of the sinudoidal phase modulation, ν_m, and 3) the baseline SNR.

In the following, a "SNR measurement" refers to the a mean SNR value computed from 100 measured holograms. The SNRs of each hologram was computed using the Fourier plane method described in Chapter II and the mean of the SNRs was used to compute the measured efficiencies that are reported in the next section.

The depth of modulation was varied by adjusting the signal amplitude from the signal generator. SNR measurements were taken at V_{in} = 500 mV_{pp}, 750 mV_{pp}, and 1000 mV_{pp}. Using (59), the calculated maximum phase shifts imparted by the EOPM corresponding to these input signal amplitudes were $\theta = 0.38\pi$, 0.55π, and 0.73π, respectively. Greater depths of modulation were inaccessible because 1000 mV_{pp} was the maximum tolerable input peak-to-peak voltage to the amplifier.

For each depth of modulation, SNR measurements were taken for modulation frequencies between 20 MHz and 100 MHz in 5 MHz increments. Frequencies below 20 MHz were inaccessible due to a 20 MHz high-pass filter in the amplifier. A SNR measurement was taken with no modulation and used as a baseline. For each depth of modulation, a baseline SNR of 100 was established prior to modulation.

For the case of $V_{in} = 1000$ mV_{pp}, two additional datasets were collected at baseline SNRs of 75 and 125.

Since the coherence efficiency, η_{coh}, is defined with respect to a perfectly monochromatic source, relative coherence efficiencies (RCE) are reported. The RCE corresponding to a specific modulation frequency is,

$$\hat{\eta}_{coh}(\nu_m) = \frac{(S/N)|_{\nu_m}}{(S/N)|_{\nu_m=0}}, \tag{64}$$

which is the ratio of the measured SNR at the modulation frequency to the baseline SNR ($\nu_m = 0$). Normalizing to the baseline SNR removes the efficiency loss incurred due to the finite linewidth of the MO.

Lastly, in addition to SNR measurements, PSDs for each depth of modulation were measured using a SFPI and used to verify that the phase modulation system was functioning as expected.

IV. Results

This chapter presents the measured PSDs and relative coherence efficiencies that were collected for each depth of modulation and at each modulation frequency. The record data are compared to the theoretical predictions discussed in Chapter II.

Power Spectral Density

In this section, the PSDs measured by the SFPI are presented and qualitatively compared to the theoretical predictions. Figure 13 (a) shows the PSDs of the unmodulated signal. Figure 13 (b-d) shows the PSDs when the source was sinusoidally phase modulated at $\nu_m = 20$ MHz for modulation depths corresponding to V_{in} =500 mV_{pp}, 750 mV_{pp}, and 1000 mV_{pp}. Each PSD is the average of 8 scans from the SFPI and each one is normalized to the strongest peak.

Figure 13 (a) shows a single peak representing the lineshape of the carrier frequency of the MO. The measured lineshape is well approximated by a Lorentzian distribution with a full-width at half-maximum of $\Delta\nu = 1$ MHz as expected, and the measured linewidth of the scan shown is approximately 1±0.1 MHz, however this value is not an accurate measurement of the linewidth. Both the laser and the SFPI are reported to have less than 1 MHz linewidth, so the measured linewidth is really the sum of the laser and SFPI linewidth, and not the laser linewidth alone.The residuals suggest asymmetry in the Lorentzian distribution of the line.

Figures 13 (b-d) show the PSDs that result from 20 MHz sinusoidal modulation at modulation depths corresponding to V_{in} =500 mV_{pp}, 750 mV_{pp}, and 1000 mV_{pp}, respectively. Amplitude scaled duplicates of the MO lineshape appear at positive and negative integer multiples of the modulation frequency. As the depth of modulation increases, more energy is transferred from the carrier to the side bands. When V_{in} =

1000 mV, the carrier is fully suppressed.

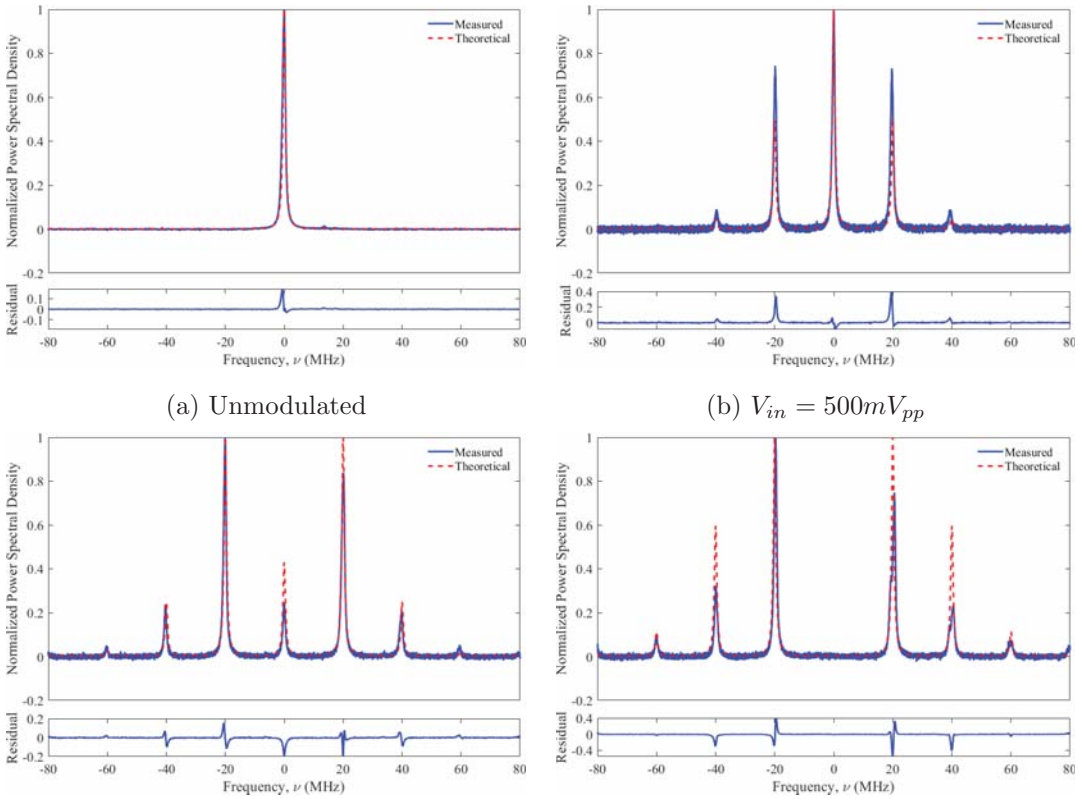

(a) Unmodulated

(b) $V_{in} = 500mV_{pp}$

(c) $V_{in} = 750mV_{pp}$

(d) $V_{in} = 1000mV_{pp}$

Figure 13. Measured and theoretical power spectral densities of the (a) unmodulated signal, (b) sinusoidally modulated signal at V_{in}=500 mV_{pp}, (c) sinusoidally modulated signal at V_{in}=750 mV_{pp}, and (d) sinusoidally modulated signal at V_{in}=1000 mV_{pp}. The solid blue lines show power spectral densities measured from a single trace of the scanning Fabry-Perot interferometer. The red dashed lines show the expected theoretical power spectral densities.

The residuals show that there are several discrepancies between the measured PSDs and the PSDs that theoretically should result from sinusoidal phase modulation. First, the relative amplitudes of the side bands deviate from the Bessel amplitudes significantly. In Figure 13 (b), the theory underestimates the measured amplitude of the first-order side band by approximately 0.26. In Figure 13 (c) and Figure 13 (d), the curves are normalized to the first order side band, but the theory overestimates the amplitude of the carrier by approximately 0.18 in Figure 13 (c), and overestimates the amplitude of the second-order side band by approximately 0.3 in Figure 13 (d).

Finally, in Figure 13 (c) and Figure 13 (d), the first-order side bands located at -20 MHz has slightly higher amplitude than the first-order side band located at +20 MHz. The actual measured values of the peaks are shown in Figure 14. These values are used to compute the theoretical curves in the following section.

These discrepancies suggest that the predicted depth of modulation computed using the values for g_{amp} and V_π provided by the manufacturers may not be completely accurate. Alternatively, imperfections in the sinusoid output of the signal generator, signal distortion caused by the amplifier, or slight misalignment of the Fabry-Perot etalon may account for the observed deviations from the theory.

	Peak Order								
Modulation Depth (mVpp)	-4	-3	-2	-1	0	1	2	3	4
500 Measured	0	0	0.09	0.74	1	0.73	0.09	0	0
500 Ideal	0	0	0.05	0.49	1	0.49	0.05	0	0
750 Measured	0.02	0.05	0.24	1	0.25	0.84	0.2	0.05	0.02
750 Ideal	0	0.02	0.25	1	0.43	1	0.25	0.02	0
1000 Measured	0.06	0.1	0.32	1	0	0.75	0.23	0.07	0.05
1000 Ideal	0.01	0.11	0.6	1	0.1	1	0.6	0.11	0.01

Figure 14. Measured Power Spectral Density Relative Peak Heights vs. Theoretical.

Since there is disagreement between the measured PSDs and the theoretical predictions, the analysis will proceed using both sets of values to analyze the measured data. The peak values predicted by the theory are what is expected of an ideal EOPM and will be referred to as the "Ideal Modulator" peak values. The peak values measured by the SFPI will be referred to as the "Fabry-Perot (FP) Measured" values.

The Visibility-Squared Model

The previous discussion of coherence theory suggests that the relative coherency should be related to the relative visibility. Assuming a polynomial relationship where

$$\hat{\eta}_{coh} = Cv^n, \tag{65}$$

where C is the proportionality constant, and n is the polynomial order, the power can be regressed from a log-log plot. Figure 15 shows that a linear function is a good fit for the log-log plot. The regression has r^2=0.9261 further suggesting a good fit. The estimated slope is m = 1.977±0.1442 and the estimated intercept is b = -0.1848±0.2250. The slope is approximately 2, and is plausibly 2 to within one standard deviation of the estimate, suggesting that the relative efficiency is proportional to the relative visibility-squared (RVS). Further, the intercept is approximately 0, and again is plausibly so to within one standard deviation of the estimate, suggesting that the proportionality constant A = 1, so the relative coherence efficiency is equal to the RVS. Moving forward, the measured data are compared against the RVS model, however the the model is computed using both the Ideal Modulator PSD peak values and the FP Measured values.

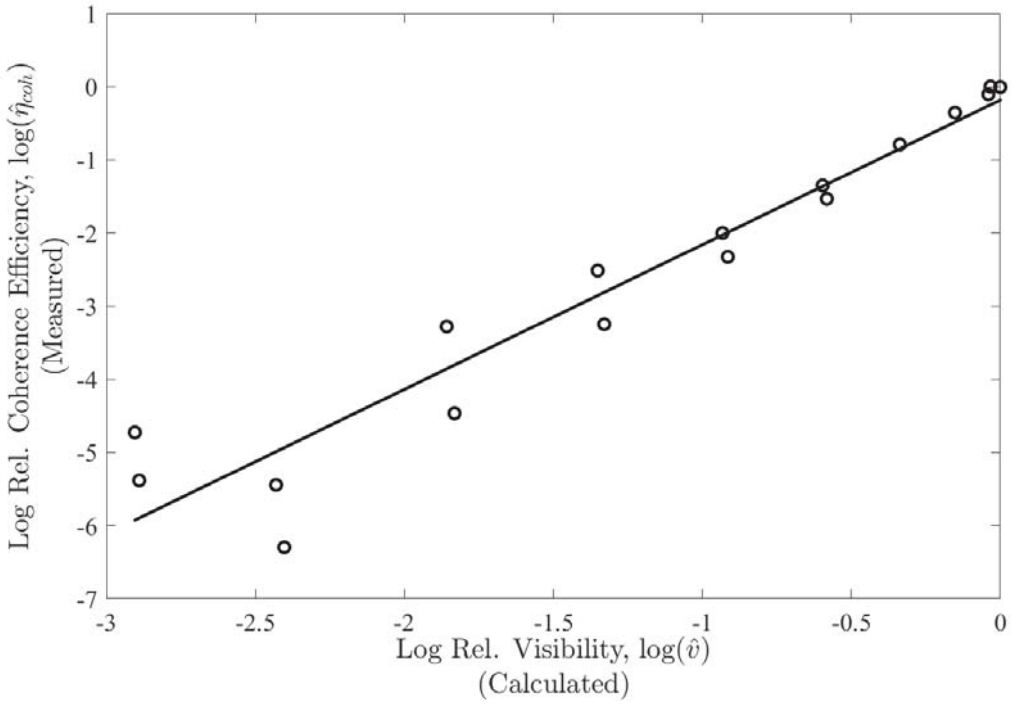

Figure 15. Log-Log Regression of Relative Coherence Efficiency vs Relative Visibility. The equation of the best fit line is y = 1.9771x-0.1848. The fit has coefficient of determination r^2 = 0.9261 suggesting a good fit to the data.

Relative Coherence Efficiency

In this section, the RCEs measured for each depth of modulation at each modulation frequency are presented. The recorded data are compared against the RVS model computed using both Ideal Modulator and FP Measured PSD peak values.

Figure 16 shows the measured RCE as a function of the modulation frequency at modulation depth corresponding to an input signal of V_{in} =500 mV_{pp} taken at a baseline SNR of 100. In addition to the measured data, both FP Measured and Ideal Modulator RVS curves are plotted.

Residuals are plotted below the RCE plot. The measured SNR of the unmodulated signal was used as the normalization baseline so its residual is 0 and it is not reported. The uncertainty in each data point is computed as the ratio of mean to standard

deviation over the 100 holograms. The average uncertainty over the 19 data points displayed in Figure 16 is 0.0091. Since the overall uncertainty was so low, error bars for individual measurements are not reported.

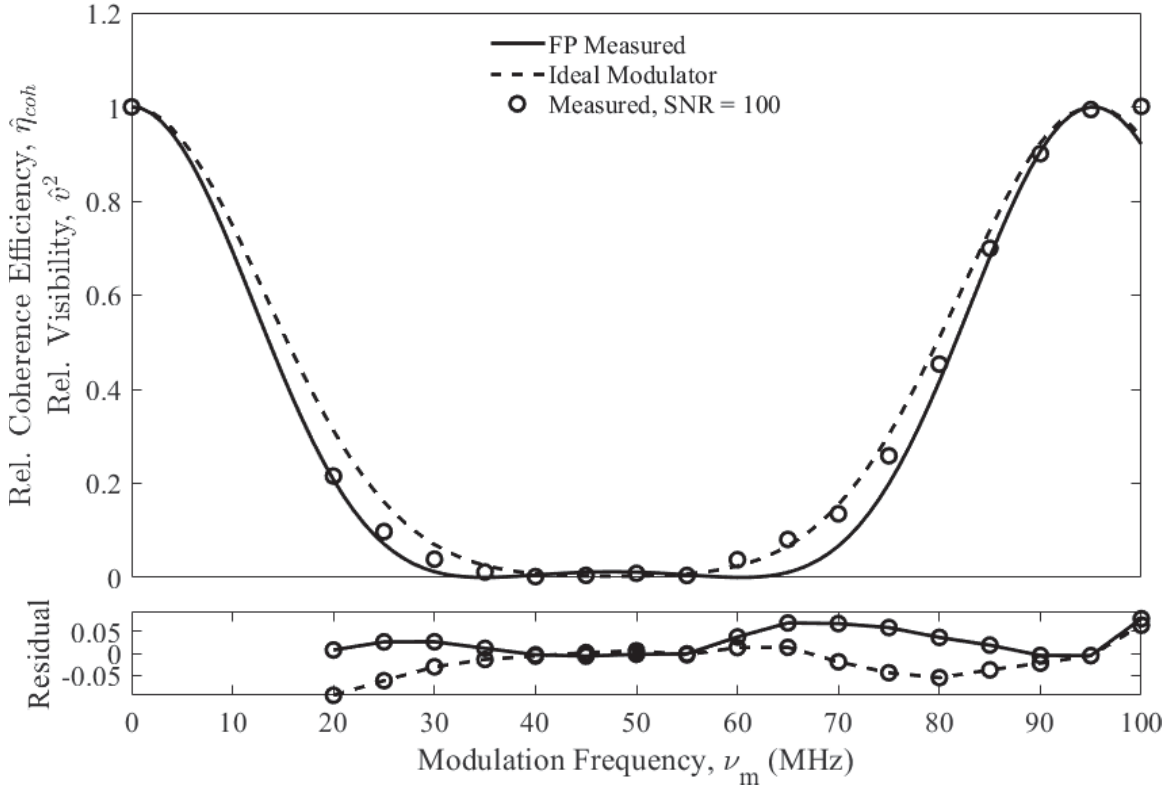

Figure 16. Relative coherence efficiency vs. phase modulation frequency at modulation amplitude V_{in} = 500 mV_{pp} and baseline SNR = 100. In addition to the measured data, both FP Measured (solid line) and Ideal Modulator (dashed line) RVS curves are plotted for an optical path length difference of 3.14 m. Residuals are plotted below.

The measured RCEs show strong agreement to both the FP Measured and Ideal Modulator predictions deviating by a root-mean-square error (RMSE) of 0.0378 for the FP Measured, and a RMSE of 0.0397 for the Ideal Modulator predictions. The residuals are not distributed normally and have some structure, which suggests that systematic errors are present.

Figure 17 shows the measured RCE as a function of the modulation frequency at modulation depth corresponding to an input signal of $V_{in} = 750mV_{pp}$ taken at a baseline SNR of 100. The average uncertainty over all the data points is 0.01. Again,

both FP Measured and Ideal Modulator predictions are plotted with the measured data. The FP Measured predictions have RMSE 0.0429 and the Ideal Modulator predictions have RMSE 0.373. The Ideal Modulator model underpredicts the measured data in the region between 35 MHz and 60 MHz, but the FP Measured predictions have greater overall RMSE. Qualitatively, the FP Measured model appears to better fit the data because it more accurately predicts the behavior of the data in the center frequencies. Again, the residuals appear to have sinusoidal structure further suggesting that systematic errors are present.

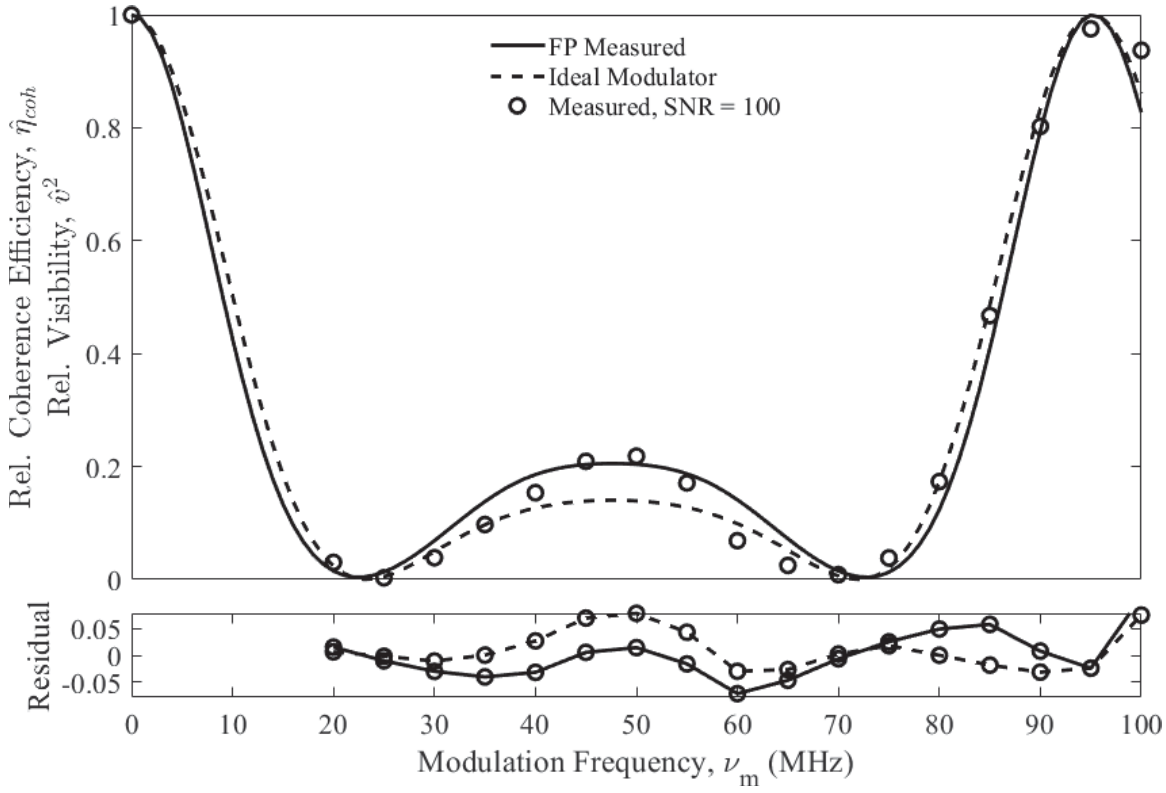

Figure 17. Relative coherence efficiency vs. phase modulation frequency at modulation amplitude V_{in} = 750 mV_{pp} and baseline SNR = 100. In addition to the measured data, both FP Measured (solid line) and Ideal Modulator (dashed line) RVS curves are plotted for an optical path length difference of 3.14 m. Residuals are plotted below.

Figure 18 shows the measured RCE as a function of the modulation frequency taken at modulation depth corresponding to an input signal of $V_{in} = 500mV_{pp}$ at baseline SNRs of 75, 100, and 125. In this scenario, where the modulation depth was

the greatest, the FP Measured predictions, which had RMSE 0.391, greatly outperformed the Ideal Modulator predictions, which had RMSE 0.1007. This suggests that the measurements taken by the SFPI are in fact accurate and that the EOPM may deviate from ideal performance at high depths of modulation. Again, the residuals appear to have similar structure to the $V_{in} = 750mV_{pp}$ case for the Ideal Modulator predictions, but are randomly distributed in for the FP Measured predictions.

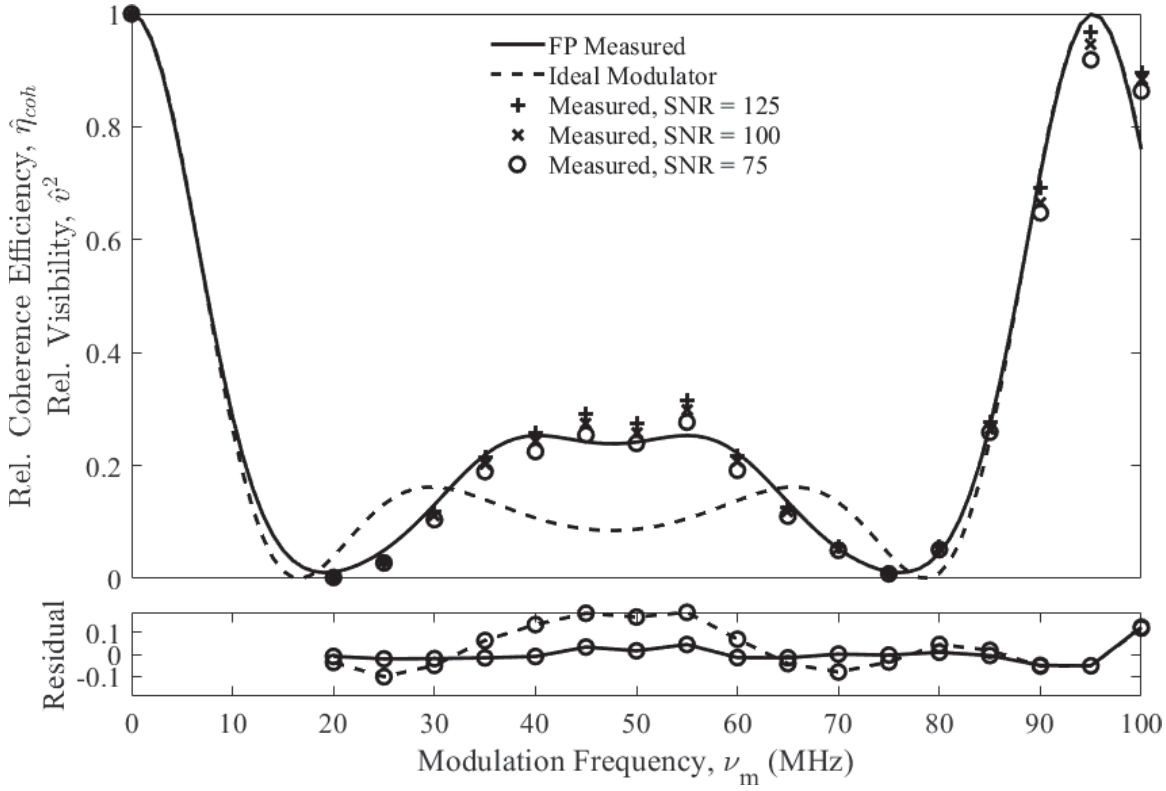

Figure 18. Relative coherence efficiency vs. phase modulation frequency at modulation amplitude V_{in} = 1000 mV_{pp} and baseline SNR = 75 (o markers), 100 (x markers), and 125 (+ markers). In addition to the measured data, both FP Measured (solid line) and Ideal Modulator (dashed line) RVS curves are plotted for an optical path length difference of 3.14 m. Residuals are plotted below.

At the greatest depth of modulation, the RCEs were also measured at 3 different baseline SNRs. The average uncertainty in the measurements at these 3 baseline SNRs are 0.0118, 0.0097, and 0.0098 for baseline SNR = 75, 100, and 125, respectively. The RCEs do not appear to depend on the baseline SNR, at least in high SNR regime,

however the data suggests that higher baseline SNR produces slightly higher RCE measurements for the same modulation frequency.

Sinusoidal phase modulation is interesting in that its effect on SNR immediately obvious. On the one hand, degrading the coherence properties of the MO using this method of modulation does degrade SNR as expected, however for certain modulation frequencies, the SNR recovers. This recoherence effect in which the SNR returned to its unmodulated value was observed for all three depths of modulation. Though the observed behavior defies common sense, it is an expected outcome when compared to the RVS model.

Discussion of Errors

In general, the measured data tended to agree with the RVS values, however for every depth of modulation the residuals were not normally distributed, and further appeared to have periodic structure. Sources of error can be separated into two categories. They are errors in the assumptions used in the model and errors in measurement.

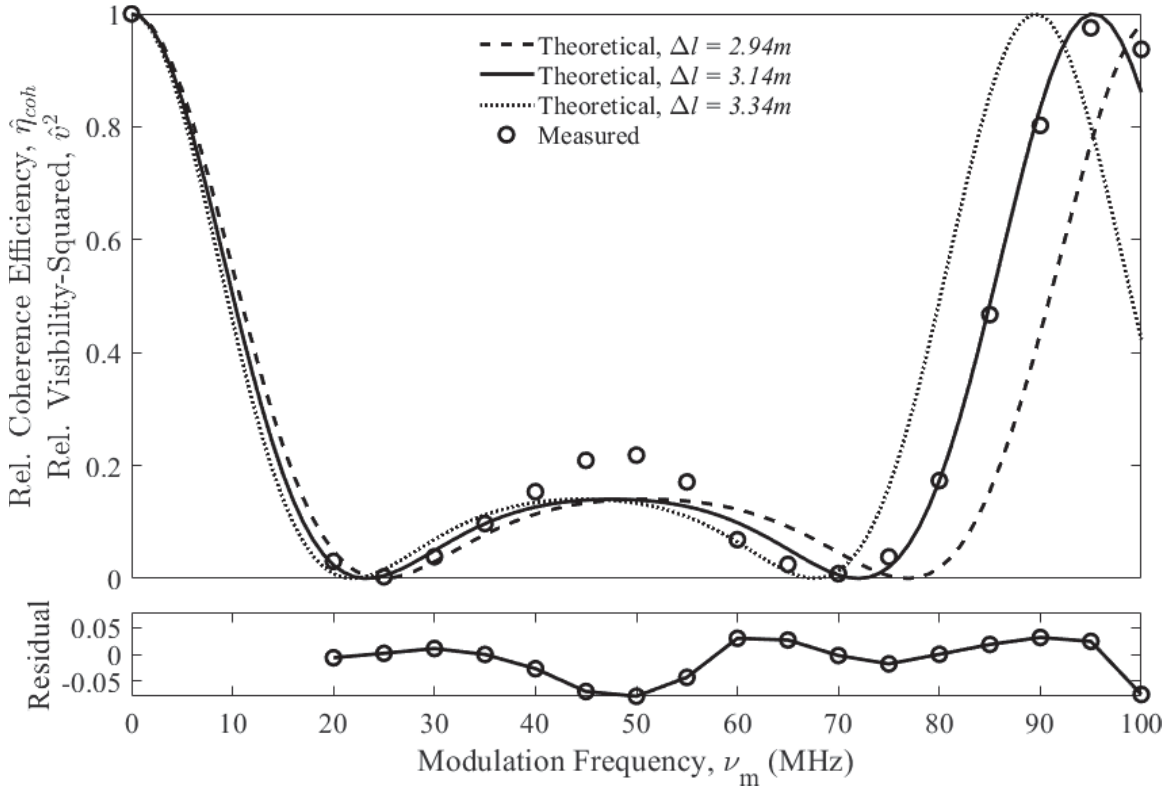

Figure 19. Relative coherence efficiency vs. phase modulation frequency at modulation amplitude V_{in} = 1000 mV_{pp} and baseline SNR = 100. RVS curves are plotted for optical path length differences of 2.94 m (dashed line), 3.14 m (solid line), and 3.34 m (dotted line). Residuals corresponding to the 3.14 m theoretical curve are plotted below.

To assess potential model errors, the parameters on which the visibility depended are revisited. The visibility depended on the lineshape of the MO, depth of modulation, frequency of modulation, and the OPD. The lineshape of the MO was assumed to be Lorentzian with linewidth of 1 MHz, however due to resolution limitations of the SFPI, a reliable measurement was never taken. If the Lorentzian lineshape assumption was accurate, then an accurate measurement of the linewidth would be unnecessary because it was calibrated out by dividing out the unmodulated efficiency (in the calculation of the relative coherence efficiency). The depth of modulation depended on values specified by the manufacturer for g_{amp} and V_π. Further, the value for V_π was extrapolated from a V_π that was specified at a different wavelength. Losses

due to propagation through transmission cables were also not included in the model. The OPD also strongly impacts the coherence efficiency, however Figure 19 shows that varying the OPD scales the frequency dimension (x-axis) rather than the efficiency dimension (y-axis). This suggests that 3.14 m is in fact a good estimate of the OPD of the DH system.

The predictions made using the FP Measured data generally outperformed the Ideal Modulator predictions, but especially so at high depths of modulation, suggesting that the modulator performance degrades at high input voltages.

Instrumentation errors are also likely to be present in the data and would explain why the measured PSDs deviated from predictions. Frequency drift of the MO was observed on the SFPI, which affected the phase shift imparted by the EOPM, but also affected the measurements taken by the SFPI. Though the EOAM was not used in this experiment, it was still present in the optical path. Since the EOAM was not anti-reflective coated for 532mn light, transmission through the EOAM deteriorated the beam quality. Multiple reflections inside the EOAM cavity were also possible. The EOAM was installed to support future DH coherence experiments and could not be removed without complete realignment of the DH system.

On activation of the analog amplifier, the EOPM was observed to slightly decrease transmissivity, even though phase modulation should not have changed the irradiance of the beam. The change in transmissivity varied by the frequency of modulation, but also varied temporally so thermal effects are suspected. Finally, the signal driving the EOPM was assumed to be a perfect sinusoid, however the signal generator likely had imperfections, and it was possible that amplifier also introduced some signal distortion.

V. Conclusion

Summary

A DH system in the off-axis IPRG was assembled and used to measure the effects of the coherence properties of the MO on SNR. The coherence properties of the MO were degraded using sinusoidal phase modulation that imparted maximum phase shifts of $0.38\pi, 0.55\pi$, and 0.73π, at modulation frequencies of 20MHz to 100MHz. While sinusoidal modulation did degrade the SNR for most modulation frequencies at every depth of modulation, the SNR was observed to recover at higher modulation frequencies. A relative visibility-squared model was regressed using the collected data and two sets of predictors were used to inform the model. The Ideal Modulator predictors were parameters computed from manufacturer specifications and represented how one would expect the modulator to alter the electric field. The FP Measured predictors were measured using a SFPI and gives another perspective intot he actual state of the electric field of the MO. In general, the FP Measured data predictions outperformed the Ideal Modulator predictions, and especially so at the greatest depth of modulation. The measured RCEs deviated from the best case theoretical RVS by RMSEs of 0.0378, 0.0373, and 0.0391 for the $0.38\pi, 0.55\pi$, and 0.73π depths of modulation, respectively. Coherence efficiencies were measured at baseline SNRs of 75, 100, and 125 at the greatest depth of modulation, and it was found that the system's baseline SNR did not significantly impact the coherence efficiency, at least in the high SNR regime.

Impact

The DH literature has extensive simulations and efficiency studies that quantify the performance of a DH system implemented in various geometries and used in

difference sensing scenarios, however no research has ever directly measured effect of coherence on SNR. The data presented in this work addresses that gap by providing empirical data collected under laboratory controlled decoherence situations. The RVS model was shown to be an effective predictor of coherence efficiency, capable of estimating the efficiency to under 4%. This information can be used to better characterize the total SNR loss due to inefficiencies in a DH system. Since the DH applications of interest typically operate in already low SNR regimes, it is critically important that the effective SNR be accurately modeled to inform system design considerations. Finally, it was shown that DH is highly sensitive to coherence effects to the point that the RCE curves were able to diagnose degraded performance in the EOPM. This suggests that DH has the potential to be used as a tool to measure the coherence of a source.

Future Work

While sinusoidal modulation does degrade the coherence properties of the MO, it does so by shifting energy from the carrier into the side bands. However, the lineshapes and linewidths of the sidebands, which is generally associated with the coherence length of the system, are still identical to the MO's. Different methods of modulation such as pseudo-random bit sequence or white Gaussian noise waveforms should be investigated since these methods have been reported to alter the MO linewidth and lineshape. These alternate modulation signals could also be applied with sinusoidal modulation to investigate the composite coherence efficiency.

The DH system used in this experiment used a CW laser as the MO. Coherence efficiency measurements should also be measured for a pulsed laser. Finally, while the empirical data used to regress the RVS model, no rigorous derivation has been performed to conclusively draw that correlation. A derivation from first principles

should be performed to establish conclusively that a quadratic relationship between the visibility and coherence efficiency truly exists.

Bibliography

1. B. Anderson, A. Flores, R. Holten, and I. Dajani. Comparison of phase modulation schemes for coherently combined fiber amplifiers. *Optics Express*, 23(21):27046, 2015.

2. B. Anderson, A. Flores, R. Holten, T. Ehrenreich, and I. Dajani. Beam combining and SBS suppression in white noise and pseudo-random modulated amplifiers. *Optics Express*, 23:93441U, 2015.

3. B. M. Anderson, A. Flores, and I. Dajani. Filtered pseudo random modulated fiber amplifier with enhanced coherence and nonlinear suppression. *Optics Express*, 25(15):17671, 2017.

4. M. T. Banet and M. F. Spencer. Spatial-heterodyne sampling requirements in the off-axis pupil plane recording geometry for deep-turbulence wavefront sensing. *Proc. SPIE*, 10410, 2017.

5. M. T. Banet, M. F. Spencer, R. A. Raynor, and D. K. Marker. Digital holography wavefront sensing in the pupil-plane recording geometry for distributed-volume atmospheric aberrations. *Proc. SPIE*, 9982, 2016.

6. J. D. Barchers, D. L. Fried, and D. J. Link. Evaluation of the performance of Hartmann sensors in strong scintillation. *Applied Optics*, 41(18):3674, 2002.

7. J. D. Barchers, D. L. Fried, D. J. Link, A. Tyler, and W. Moretti. Performance of wavefront sensors in strong scintillation. *Proceedings of SPIE*, (4839), 2003.

8. D. Claus, D. Iliescu, and J. M. Rodenburg. Coherence requirement in digital holography. *Applied Optics*, 52(1):A326–A335, 2013.

9. N. Demoli, J. Mestrović, and I. Sović. Subtraction digital holography. *Appl. Opt.*, 42(5):798–804, Feb 2003.

10. D. Fink. Coherent Detection Signal-to-Noise. *Appl. Opt.*, 14(3):689–690, mar 1975.

11. D. Gabor. A new microscopic principle. *Nature*, 161(777), 1948.

12. P. Gatt and D. Jacob. Coherent integration efficiency, diversity and detectivity of temporally integrated random coherent ladar signals. *Laser Radar Technology and Applications Xv*, 7684, 2010.

13. J. W. Goodman and R. W. Lawrence. Digital image formation from elecronically detected holograms. *Applied Physics Letters*, 11(3):77, 1967.

14. E. Hecht. *Optics*. Pearson Education, Inc, 5th edition, 2017.

15. J. C. Marron. Coherent Imaging. *Image (Rochester, N.Y.)*, (1):2–4, 2010.

16. J. C. Marron, R. L. Kendrick, N. Seldomridge, T. D. Grow, and T. A. Höft. Atmospheric turbulence correction using digital holographic detection : experimental results. *Opt. Express*, 17(14):207–211, 2009.

17. J. C. Marron, R. L. Kendrick, S. T. Thurman, N. L. Seldomridge, T. D. Grow, C. W. Embry, and A. T. Bratcher. Extended-range digital holographic imaging. *Proc. SPIE*, 7684:2–7, 2010.

18. C. J. Pellizzari, M. T. Banet, M. F. Spencer, and C. A. Bouman. Demonstration of single-shot digital holography using a Bayesian framework. *J. Opt. Soc. Am. A*, pages 1–5, 2017.

19. C. J. Pellizzari, M. F. Spencer, and C. A. Bouman. Phase-error estimation and image reconstruction from digital-holography data using a bayesian framework. *J. Opt. Soc. Am. A*, 34(9):1659–1669, Sep 2017.

20. T.-C. Poon and J.-P. Liu. *Introduction to Modern Digital Holography with Matlab*. Cambridge University Press, New York, 2014.

21. M. F. Spencer. Spatial Heterodyne. *Encyclopedia of Modern Optics II, Volume IV*, pages 369–400, 2018.

22. M. F. Spencer, I. V. Dragulin, D. S. Cargill, and M. J. Steinbock. Digital holography wave-front sensing in the presence of strong atmospheric turbulence and thermal blooming. *Proc. SPIE*, 9617, 2015.

23. M. F. Spencer, R. A. Raynor, M. T. Banet, and D. K. Marker. Deep-turbulence wavefront sensing using digital-holographic detection in the off-axis image plane recording geometry. *Opt. Eng.*, 56(3), 2016.

24. M. F. Spencer and D. E. Thornton. Signal-to-noise models for digital- holographic detection. *Proceedings of SPIE*, 1065, 2018.

25. D. E. Thornton, M. F. Spencer, and G. P. Perram. Deep-turbulence wavefront sensing using digital holography in the on- axis phase shifting recording geometry. *Proc. SPIE*, 10410(September 2017), 2017.

26. D. E. Thornton, M. F. Spencer, C. A. Rice, and G. P. Perram. Efficiency measurements for a digital-holography system. *Proc.SPIE*, 10650:10650 – 10650 – 10, 2018.

27. S. T. Thurman and J. R. Fienup. Correction of anisoplanatic phase errors in digital holography. *J. Opt. Soc. Am. A*, 25(4):995–999, apr 2008.

28. E. Wolf. *Introduction to the Theory of Coherence and Polarization of Light*. Cambridge University Press, New York, 2007.